Bachelor Thesis

Isotope Effect on Structure and Magnetic Properties in Spin Crossover Complexes

Faculty of Mathematics and Natural Sciences
University of Cologne

Bachelor of Science in Chemistry

presented by
Wanqing Chen

Cologne, Dec. 2024

Eidesstattliche Erklärung

Hiermit versichere ich, Wanqing Chen, an Eides statt, dass ich die vorliegende Arbeit mit dem Thema

" Isotope Effect on Structure and Magnetic Properties in Spin Crossover Complexes"

selbstständig und ohne die Benutzung anderer als der angegebenen Hilfsmittel angefertigt habe.
Alle Stellen, die wörtlich oder sinngemäß aus veröffentlichten und nicht veröffentlichten Schriften entnommen wurden, sind als solche kenntlich gemacht.
Die Arbeit ist in gleicher oder ähnlicher Form oder auszugsweise im Rahmen einer anderen Prüfung noch nicht vorgelegt worden.
Ich versichere, dass die eingereichte elektronische Fassung der eingereichten Druckfassung vollständig entspricht.

_____

(Ort, Datum)

_____

(Unterschrift)

Table of Contents

Abstract

Isotope effects can significantly influence the magnetic properties of materials, as observed in various studies. This research focuses on magnetic materials derived from transition metal complexes, specifically examining a $3d^6$ iron complex that exhibits spin crossover (SCO) behavior. The spin crossover phenomenon involves a cooperative transition between low-spin (LS) and high-spin (HS) states, which is characterized by a sudden switch accompanied by thermal hysteresis. Interestingly, the spin crossover behavior varies between different polymorphs: while the orthorhombic polymorph shows an abrupt transition, the monoclinic polymorph displays a more gradual transition. This study further explores how isotope substitution affects the structural and physical properties of these materials, providing new insights into their magnetic behavior. The compound $[Fe(PM\text{-}BiA)_2(NCS)_2]$, *cis*-bis(thiocyanato)-bis(N-2'-pyridylmethylene)-4-(aminobiphenyl)-iron(II), as a typical SCO compound, crystallizes in two polymorphic forms, orthorhombic and monoclinic, providing an excellent platform to explore how isotope effects influence both structure and magnetic properties.

The study is divided into two parts:

- In the first part, a feasible isotopic substitution path was carried out to synthesize two polymorphs of $[^{57}Fe(PM\text{-}BiA)_2(NCS)_2]$, with the naturally abundant ^{nat}Fe substituted by Fe enriched in the isotope ^{57}Fe. To achieve a relatively higher yield of different polymorphs, ^{nat}Fe was used to synthesize the polymorphs under varying reaction conditions, allowing the selection of appropriate reaction conditions for application.
- The second part focuses on deuteration of $[Fe(PM\text{-}BiA)_2(NCS)_2]$. In this study, an Anderson-type polyoxometalate, $[NH_4]_3[CrMo_6O_{18}(OH)_6]\cdot 7H_2O$, was utilized as a catalyst for the oxidation of 2-picoline into N-2'-pyridylmethylene.

Based on magnetic susceptibility measurements and Powder X-Ray diffraction (PXRD) characterization of $[^{57}Fe(PM\text{-}BiA)_2(NCS)_2]$, it was observed that the isotope effect introduced by substituting with ^{57}Fe caused only minor changes in the structure and magnetic behavior compared to the non-substituted compound. However, the attempted oxidation of 2-picoline using the proposed method did not yield successful results under the current conditions.

1. Introduction

1.1 Spin Crossover (SCO)

Spin crossover (SCO) usually occurs in 3d transition metal complexes where the spin states can switch between low-spin (LS) and high-spin (HS) states under changes in external conditions such as temperature, pressure, and light.[1] It was first discovered in 1931 by Cambi and Szego.[2] Approximately 30 years after Baker and Bobonich first discovered the SCO phenomenon in iron(II) coordination compounds, a growing number of iron(II) and iron(III) SCO complexes began to emerge. [3,4] In fact, it was until the 1980s that scientists realized that iron(II) complexes, due to their molecular bistability, could be used as active components in magnetic storage devices. Molecular bistability refers to the property of a molecular structure to switch between two different, mutually stable states. Both states can remain stable under specific external conditions, such as temperature, light, electric fields, or magnetic fields. The transition process between these states can be reversible.[5] Due to the transition between the HS and LS states, accompanied by changes in electronic configuration and magnetism, the spin state transition of SCO materials can be used to manipulate the material's magnetism. This reversible transition of magnetism demonstrates the potential of SCO materials in storage media and sensor applications.[6]

In this study, our objective is to investigate SCO in Fe(II) compounds with a $3d^6$ electron configuration (*Figure 1*). In the HS state, the electron configuration is $t_{2g}^4e_g^2$ with four unpaired electrons in t_{2g} and two in the e_g orbitals and a total spin $S = 2$. In contrast, in the LS state, the electron configuration is $t_{2g}^6e_g^0$, and all electrons occupy the lower-energy t_{2g} orbitals, resulting in a total spin $S = 0$. The transition between these two states involves an intra-ionic electron transfer between the t_{2g} and e_g orbitals.[7]

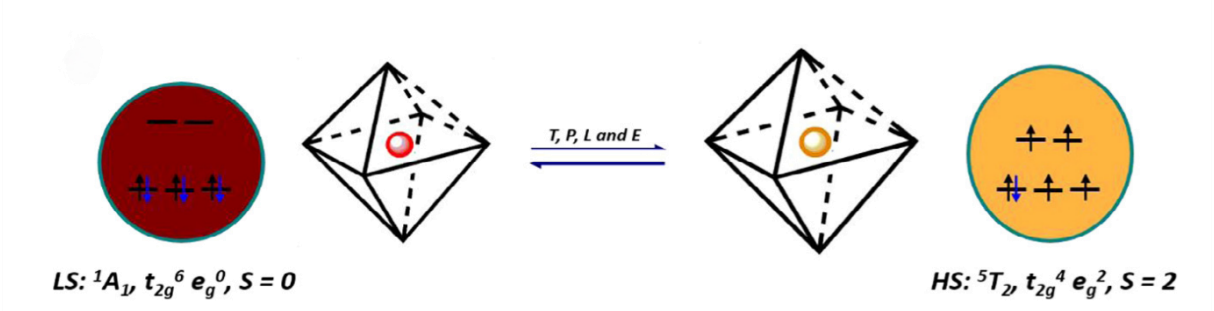

Figure 1. Spin crossover phenomenon in a $3d^6$ electron configuration complex: On the left, the deep red circle contains an Fe(II) ion in an octahedral environment in the LS state with three electron pairs, resulting in $S = 0$. On the right, the pale yellow circle represents the Fe(II) ion in the HS state with one pair of electrons and four unpaired electrons, resulting in $S = 2$. Figure 1 is taken from Ref. [8].

SCO curves are used to illustrate different spin transition behavior, representing the relationship between the fraction of molecules in HS state (γ_{hs}) and temperature. $T_{1/2}$ is the temperature is defined as the point at which $\gamma_{hs} = 0.5$, representing the point where half of the molecules are in the high-spin state.[9] Cooperative interactions between spin-crossover molecules during spin transitions significantly influence the shape of the SCO curves in solid-state SCO compounds. These interactions often result in abrupt transitions or hysteresis loops.[9] Spin transitions are generally divided into five types (*Figure 2*).

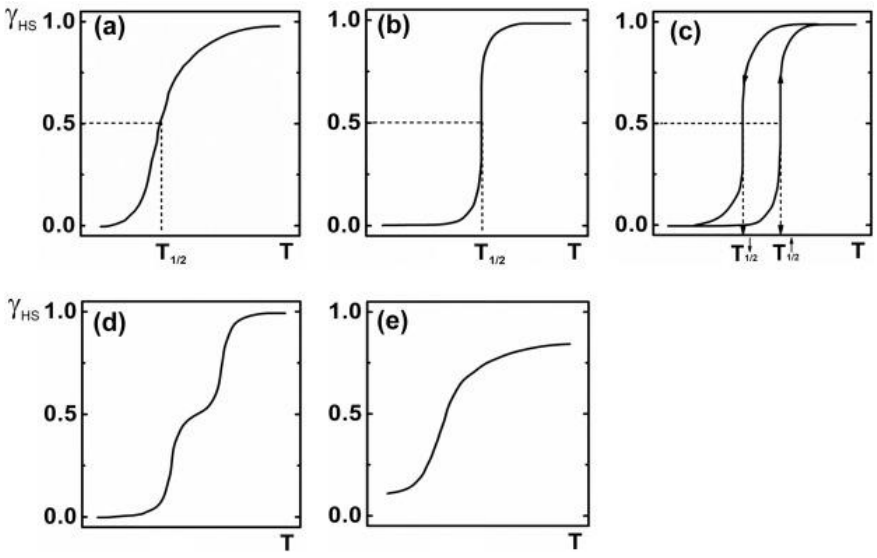

Figure 2. The five main types of spin transition curves are: a) Gradual spin transition. b) Abrupt spin transition. c) Spin transition with hysteresis. d) Two-step spin transition. e) Incomplete spin transition. Figure 2 is taken from Ref. [9].

1. Gradual spin transition (*Figure 2a*): The transition between spin states occurs smoothly over a wide temperature range, showing no abrupt changes or discontinuities. Gradual spin transitions, where the spin crossover curve follows Boltzmann distribution law, can appear in either liquid or solid states, with almost no or only weak cooperative interactions present between molecules.[9,10]
2. Abrupt spin transition (*Figure 2b*): Due to strong cooperative interactions, molecules rapidly switch from one spin state to another, causing a phase change within a very narrow temperature range.[11]
3. Spin transition with hysteresis (*Figure 2c*): Hysteresis refers to the different spin states during a heating and cooling cycle, forming a closed loop. There are two critical temperatures, $T_{1/2}\uparrow$ for heating and $T_{1/2}\downarrow$ for cooling. This characteristic behavior implies a memory effect in the system.[12]
4. Two-step spin transition (*Figure 2d*): As temperature increases, the system first changes from a low-spin state to an intermediate spin state, and then from the intermediate spin

state to a high-spin state. This is common in multinuclear structures (SCO complexes with multiple metal ions).[13]

5. Incomplete spin transition (*Figure 2e*): The curve shows that the spin state transition does not reach 100%, with some molecules not changing spin states throughout the investigated temperature range. This phenomenon is particularly common in dinuclear compounds. The cooperativity within or between these small clusters is minimal.[14]

The SCO complex [Fe(PM-Bia)$_2$(NCS)$_2$], *cis*-bis(thiocyanato)-bis(N-2'-pyridylmethylene)-4-(aminobiphenyl)-iron(II) in this study is a widely researched material.[13] This complex primarily exists in two different polymorphs (*Figure 3*). One crystallizes in an orthorhombic structure with space group *Pccn*, and the other one in a monoclinic structure with space group $P2_1/c$.

- The orthorhombic polymorph exhibits an abrupt SCO transition around 173 K within a narrow 1 K temperature interval, accompanied by a thermal hysteresis of 5 K.[15]
- The monoclinic polymorph demonstrates a gradual SCO transition with $T_{1/2}$ at approximately 207 K, spanning a wide temperature range from 175 K to 250 K.[16]

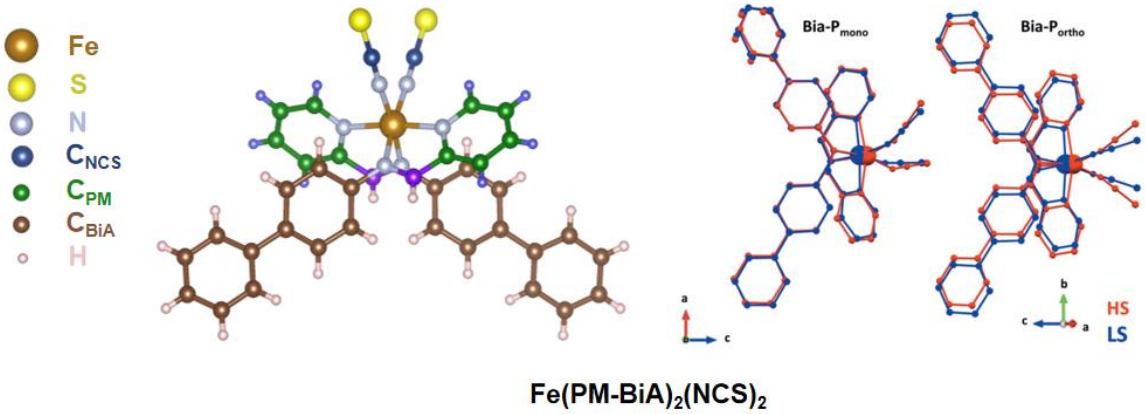

Figure 3. (Left) The molecular structure of [Fe(PM-BiA)$_2$(NCS)$_2$]. (Right) Individual molecules of [Fe(PM-BiA)$_2$(NCS)$_2$] in the two polymorphs. They are displayed in their high-spin (HS, red) and low-spin (LS, blue) states: (left) monoclinic polymorph and (right) orthorhombic polymorph. Figure 3 is taken from Ref. [6].

1.2 Ligand Field Theory (LFT)

Fe(II) with $3d^6$ electron configuration in the SCO compound is presented in *Figure 1.* The strength of the ligand field affects the arrangement of the metal ion's electron orbitals (*Figure 4*). Spin pairing energy (*P*) is defined as the total energy required to pair two electrons in the same orbital. When two electrons occupy the same orbital, they must have opposite spins due to the Pauli Exclusion Principle, resulting in an increase in energy. Additionally, an increase in energy is also caused by electron-electron electrostatic repulsion.[19] The crystal field splitting

energy (Δ_o) is defined as the energy difference that results when d-orbitals in octahedral symmetry are split into two sets of orbitals with different energies.

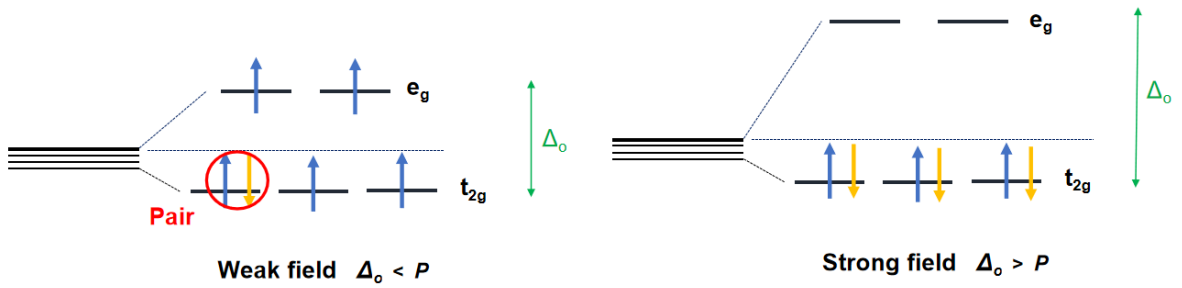

Figure 4. Diagrams of $3d^6$ electron configurations under octahedral ligand field with weak (left) and strong ligand field (right). Here, Δ_o is the crystal field splitting energy and P is the electron pairing energy.

In a weak ligand field, the energy Δ_o is lower than P. According to Hund's rule, electrons then first fill the lower energy t_{2g} orbitals, and then the higher energy e_g orbitals are filled.[18] With four electrons in the t_{2g} orbitals and two in the e_g orbitals, a configuration of $t_{2g}^4e_g^2$ is achieved. This results in paramagnetism and a high-spin state.

In a strong ligand field, Δ_o increases and exceeds P. The energy of the e_g orbitals is significantly increased by the strong ligand effect, enlarging the energy difference between the low and high energy orbitals.[10] Consequently, Hund´s rule is violated and the t_{2g} orbitals are fully occupied by six electrons, while the e_g orbitals are empty, resulting in a $t_{2g}^6e_g^0$ configuration. This leads to diamagnetism and a low-spin state in the complex.

The spin transition in SCO complexes is arising from the dependency of metal-ligand distances on ligand field strength and the complicated interaction between this dependency and electron-electron repulsion.[17] The distance between metal and ligands influences the strength of the ligand field, thus affecting Δ_o.

In the compound $[Fe(PM\text{-}Bia)_2(NCS)_2]$, the ligands PM-BiA and NCS^- are both considered medium field strength ligands in the spectrochemical series (*Figure 5*). This moderate field strength helps induce SCO behavior within a specific temperature range, allowing the iron center to transition between LS and HS.[19]

Weak Field (Low Δ_o) : $I^- < Br^- < S^{2-} < SCN^- < Cl^- < NO_3^- < F^- < C_2O_4^{2-} < H_2O <$ NCS$^-$ < $CH_3CN <$ *Pyd*, $NH_3 <$ en < *bipy* < phen < $NO^{2-} < PPh_3 < CN^- <$ CO Strong Field (High Δ_o)

Figure 5. A spectrochemical series, ligand field strength of ligands from weak field (low Δ_o) to strong field (high Δ_o). The ligands highlighted in blue are the ligands contained in $[Fe(PM\text{-}Bia)_2(NCS)_2]$.

1.3 Isotope Effect

The isotope effect on SCO complexes often changes their physical and chemical properties and has been observed in various studies. In the field of materials science, the isotope effect describes the phenomenon where the properties of a material are altered when one or more of its atoms are replaced by specific isotopes.[20]

For example, in $Fe(C_5H_5N)_2[Ni(CN)_4]$, isotope substitutions with D and ^{15}N shift the spin transition significantly to lower temperatures due to the increased isotope mass, moving it from 202 K to 194 K.[21] In $[Fe(2\text{-pic})_3]Cl_2 \cdot Sol$ (2-pic = 2-picolylamine, Sol = C_2H_5OD and CH_3OD), the transition temperature for the spin transition of iron(II) increases by 15 K on deuteration compared to the non-deuterated compound.[22] In a partially deuterated SCO complex $[FeL_2][BF_4]_2$ (L = 2,6-di(pyrazol-1-yl)pyridine), the SCO transition occurs at 257 K for deuterated samples and 262 K for protonated samples, with both samples exhibiting the same hysteresis width of 4 K. Additionally, the thermal effects and structural stability of partially deuterated $[FeL_2][BF_4]_2$ change. Deuteration affects the lattice parameters during the SCO phase transition due to the substitution of the smaller hydrogen atoms with the larger deuterium, altering internal bonding.

In the study of the SCO complex $[Fe(H_2B(pz)_2)_2(phen)]$ (pz = pyrazolyl, phen = 1,10-phenanthroline), changes in the lattice dynamics related to the spin transition were investigated through Mössbauer-based nuclear inelastic scattering, examining metal isotope substitution with the isotope ^{57}Fe replacing naturally abundant iron, ^{nat}Fe. The results show that the isotope effect significantly influences the vibrational spectrum, causing notable frequency shifts.[24] Probes substituted with ^{57}Fe isotopes can also be used to investigate the isotope effect on the structure and properties of SCO complexes through quasielastic Mössbauer absorption techniques.[25]

1.4 X-ray Scattering Principle

X-ray scattering is a powerful analytical technique used to study the structure and properties of materials at the atomic and molecular scale. When X-rays interact with a material, they are deflected by the electron clouds of atoms, resulting in a scattering pattern that carries information about the spatial arrangement of atoms within the sample.[26]

Bragg's law is typically used to describe the diffraction conditions of X-rays in the crystal (*Figure 6*). This law states that constructive interference of the scattered X-rays occurs when the path difference of the incident X-rays equals an integer multiple of the lattice spacing, resulting in diffraction peaks in the diffraction pattern.[28,29]

$$n\lambda = 2dsin\theta \quad (1)$$

λ is the wavelength of the X-rays, d is the distance between atomic planes in the crystal lattice,

θ is the angle between the incident wave and the scattering plane, n is the order of diffraction.

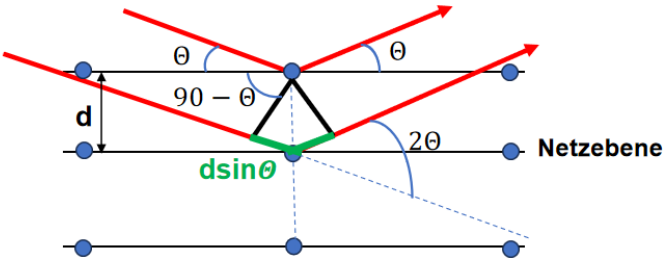

Figure 6. Illustration of the Bragg Reflection Condition.

Using the Bragg equation, the peak positions can be theoretically calculated. The relationship between the interplanar spacing *d* and the lattice parameter a depends on the crystal system and the Miller indices. For cubic systems, the *Formula 1a* is given as following. For other crystal systems, the expression depends on the specific unit cell geometry, such as tetragonal or orthorhombic systems.[27]

$$d = \frac{a}{\sqrt{h^2 + k^2 + l^2}} \tag{1a}$$

a is the lattice parameter, d is the interplanar spacing, h, k, l are the Miller indices.

To better understand the peak intensities in X-ray diffractometer (XRD) patterns, the concepts of structure factor and form factor are introduced.[27] In crystal diffraction, the structure factor *F*(*hkl*) describes the amplitude and phase of waves diffracted from lattice planes characterized by Miller indices.[34] The intensity of the diffracted beam is proportional to the square of the structure factor. The structure factor represents the total wave produced by the collective scattering (diffraction) of all atoms within the cell in a given spatial direction.[30] Thus, the structure factor can be used to obtain information about the positions of atoms within the crystal. The structure factor *F*(*hkl*), can be mathematically expressed as:[29,30]

$$F(hkl) = \sum_j f_j * e^{-2\Pi i(hx_j + ky_j + lz_j)} \tag{2}$$

$F(hkl)$ is the structure factor, f_j is the atomic scattering factor, x_j, y_j, z_j are the coordinates of this atom within the unit cell, h, k, l are Miller indices of the crystallographic plane.

The form factor describes the scattering strengths of an atom. The amplitude of X-rays scattered at position r is proportional to the electron density $\rho(r)$ at position r.[31] The electron distribution around atoms or ions is approximated by spherical symmetry. The form factor can be defined as:[32]

$$f = \int e^{-iqr} \rho(r) dr \tag{3}$$

r is the position vector from the nucleus to the electron cloud, $\rho(r)$ is the electron density at position r, q is the scattering vector.

1.5 Magnetism

In magnetic materials, various spin arrangements give rise to a wide range of magnetic properties. Making use of these properties, magnetic materials have been widely applied in fields such as electronic devices, magnetic sensors, and radio communications.[34]

There are five types of magnetism (*Figure 7*): diamagnetism, paramagnetism, ferromagnetism (FM), antiferromagnetism (AFM) and ferrimagnetism (FIM).[34]

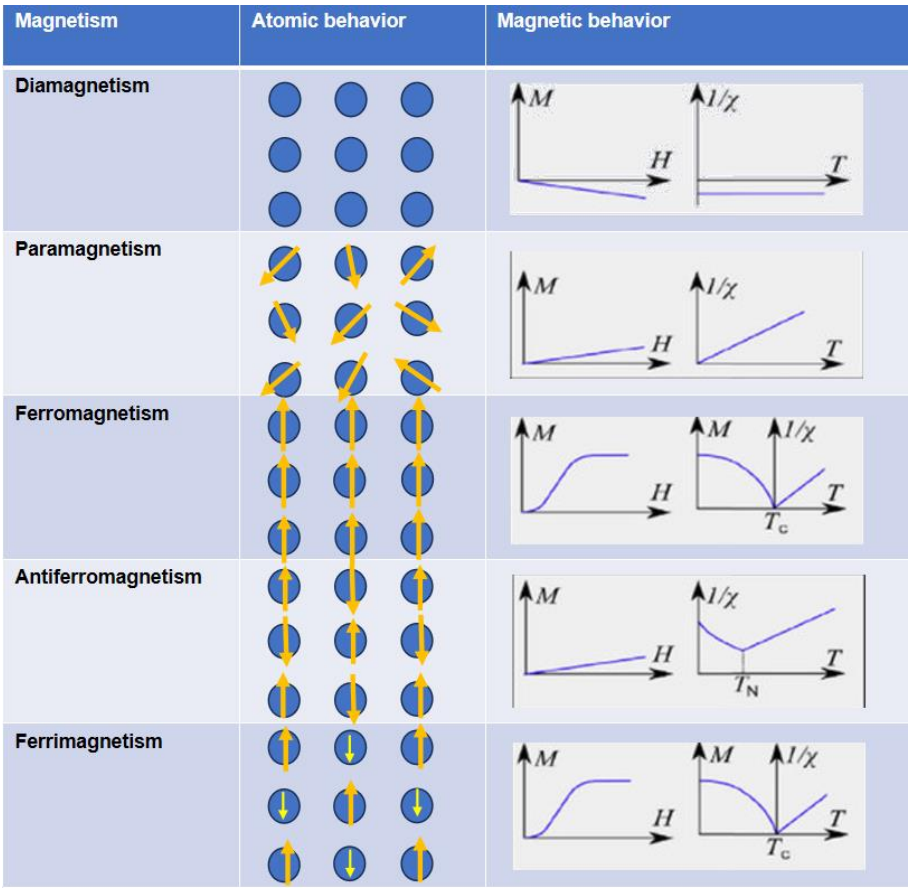

Figure 7. Main types of magnetism and their atomic and magnetic behavior. Figure 7 is taken from Ref. [39].

Paramagnetism is due to the unpaired electrons. Diamagnetism occurs when all electrons are paired.[35] The difference between paramagnetism and diamagnetism lies in the behavior of magnetic moments when there is no external magnetic field. In diamagnetic materials, internal magnetic moments completely disappear in the absence of a magnetic field. In contrast, paramagnetic materials retain magnetic moments that orient randomly due to thermal fluctuations. When a magnetic field is applied, the moments in paramagnetic materials begin to align parallel to the field, whereas diamagnetic materials develop magnetic moments in the opposite direction of the applied field.

The magnetization of the material is directly proportional to the applied magnetic field.[38] In ferromagnetic materials, when no external magnetic field is applied, the magnetic moments are aligned in the same direction. Under an external magnetic field, the magnetic dipole

moments align parallel to each other and in the same direction as the field. In antiferromagnetic materials, when no magnetic field is applied, adjacent magnetic moments are equal in magnitude but opposite in direction, aligning antiparallel to each other.[37,38] Ferrimagnetism exists only in compounds, where some magnetic moments align parallel, while others align antiparallel. However, the magnitudes of magnetic moments in the two directions are unequal. Compared to ferromagnetic materials, ferrimagnetic materials have lower magnetization.[33]

To characterize the magnetism of a material, the concept of magnetic susceptibility χ was introduced.[35] Materials that are paramagnetic always have a positive magnetic susceptibility ($\chi > 0$), while diamagnetic materials always have a negative magnetic susceptibility ($\chi < 0$). [36] Magnetic susceptibility relates to the strengths of the material's magnetization M in response to an applied magnetic field strength H:[35]

$$M = \chi H \tag{4}$$

In 1895, the French physicist Pierre Curie proposed that the susceptibility of paramagnetic materials is inversely proportional to the absolute temperature T.[40] This approximate relationship is known as Curie's Law (*Figure 8*), where C is the Curie Constant:[41]

$$\chi = \frac{C}{T} \tag{5}$$

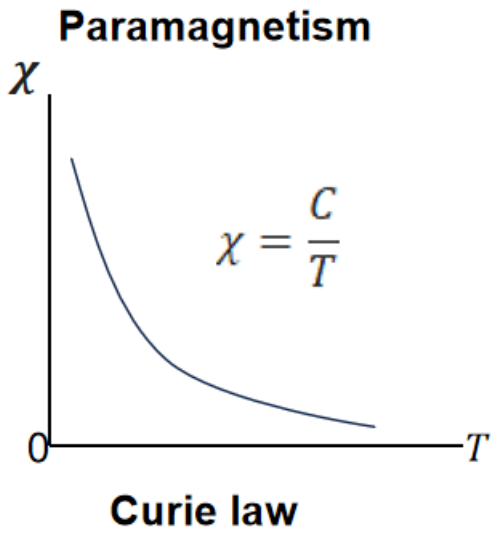

Figure 8. Diagram illustrating Curie's Law.

2. Characterization Techniques and Instruments

2.1 Powder X-ray Diffraction (PXRD)

Powder X-ray Diffraction (PXRD) was utilized to characterize the synthesized non-crystalline (powder) materials. Through PXRD measurements, a diffraction pattern can be recorded on a detector, which contains information of the intensity plotted against the Bragg angle (2θ). The position of the peaks contains information about the interplanar lattice spacings, and thus about the lattice parameters. The intensity of individual peaks is related to the structure factor and contains information about the position of the atoms in the unit cell.[42]

In an X-ray diffraction experiment, X-rays generated from a source pass through a monochromator and impinge onto the sample. With a goniometer, the angle of incidence is varied, allowing the scattered X-rays from the sample to be detected at different angles by an X-ray detector. Each particle within the sample window is penetrated by the X-ray beam in multiple possible directions, resulting in diffracted beams that strike the imaging plate at specific angles (*Figure 9*). The captured diffraction pattern provides structural information, including crystallinity, chemical composition, crystal structure, and crystal size. The collected data are further processed and analyzed using specialized software such as *Jana 2006*.[43]

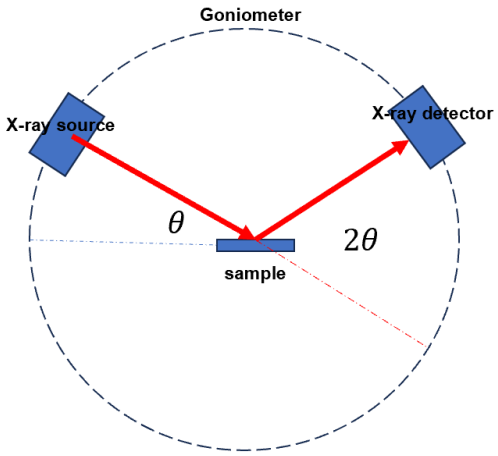

Figure 9. Illustration of the working principle the XRD used in the analysis.

The data used in this study were collected from two different PXRD machines: the STOE and the xHuber (*Figure 10*). The primary components of the X-ray diffractometer include an X-ray generator tube, a high energy electrons source, sample holder, monochromator and an X-ray detector. The STOE PXRD transmission geometry is a hybrid of the Scherrer and the Guinier camera. It uses a focused Mo K_α X-ray source with a wavelength of 0.71073 Å. Additional components of the system include a Gandolfi sample holder and a capillary sample holder. This configuration is particularly effective for measuring small sample quantities (in the mm^3 range) and is ideal for handling air-sensitive or toxic materials.[48]

The xHuber PXRD is equipped with a Cu-K_α X-ray source (λ = 1.5406 Å), a sample platform, and a G670 Guinier camera detector.[45]

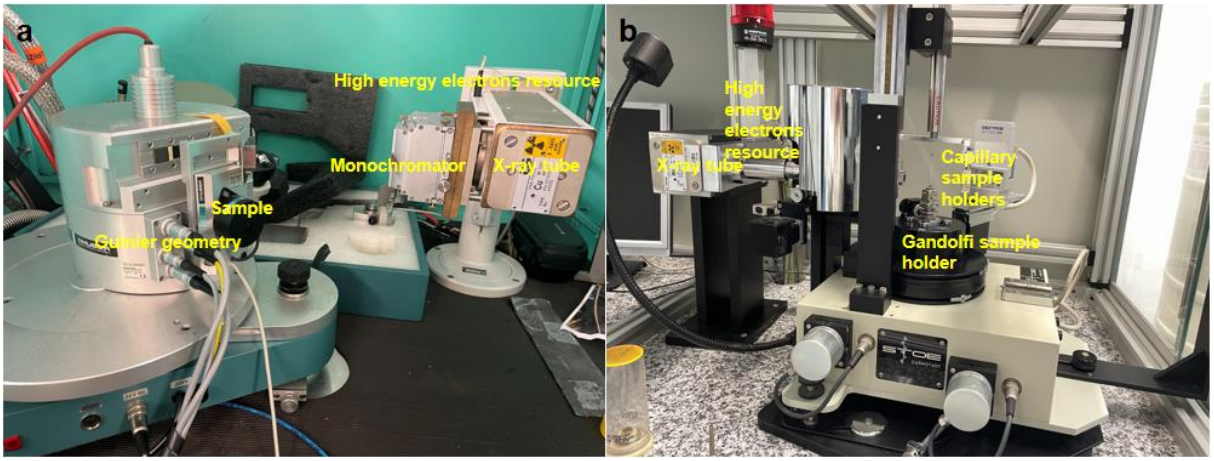

Figure 10. Construction and important components of the xHuber from JCNS-2 Lab (a) and STOE from the Inorganic Chemistry Lab, University of Cologne (b).

The sample preparation for the measurements was carried out as follows for the two machines. For the STOE machine, powder samples were carefully poured into the open end of a capillary tube. The capillary was then placed inside a glass tube, which was continuously tapped to ensure the powder fully entered and evenly filled the capillary. A segment of about 5 to 6 cm of the capillary was then cut, and the open end was sealed with wax to prevent air exposure. Finally, the sealed capillary was mounted onto the capillary sample holder for measurement (*Figure 11a*).

For the xHuber, the sample powder was evenly spread in the center of the mold, which was pre-lined with a first layer of film. A drop of methanol was then added to the center of the sample and the sample was allowed to dry completely. A second layer of film was then placed over the sample. The metal disc corresponding to the mold was pressed tightly to ensure the film was fully stretched. Excess film was removed before measurement. The sample is then secured with a metal disc and subsequently inserted into the sample holder (*Figure 11b*).

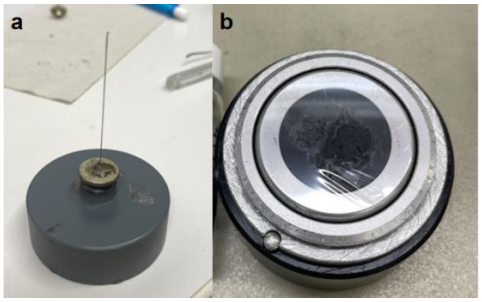

Figure 11. Prepared samples as used for powder X-ray diffraction (PXRD) measurement, for the (a) STOE and (b) xHuber diffractometer.

2.2 Magnetic Susceptibility Measurements by Quantum-Design Physical Property Measurement System (PPMS)

A Physical Property Measurement System (PPMS) is an automated low-temperature and magnet system designed for precise measurements of various physical properties of materials.[46] The Vibrating Sample Magnetometer (VSM) of the PPMS can measure the magnetization and magnetic susceptibility of a sample. The working principle of the VSM (*Figure 12*) is based on the sample undergoing vibrations at a defined frequency, driven by an electromagnetic or mechanical device within a constant magnetic field. As the sample moves up and down, its magnetic dipole moment changes, thereby altering the surrounding magnetic field.[47] According to Faraday's Law, an electromotive force (voltage) is induced in a set of pickup coils. The voltage signal is amplified by a Lock-in-amplifier. The mathematical expression of this law is as follows:[48,49]

$$\boldsymbol{\varepsilon(coil) = -\frac{d_{\phi_B}}{d_t}} \qquad (6)$$

$\boldsymbol{\varepsilon}$ is the induced electromotive force (voltage), with the unit of volts (*V*), $\boldsymbol{\phi_B}$ is the magnetic flux passing through the coil, with the unit of webers (Wb), $\frac{\boldsymbol{d_{\phi_B}}}{\boldsymbol{d_t}}$ represents the rate of change of magnetic flux over time.

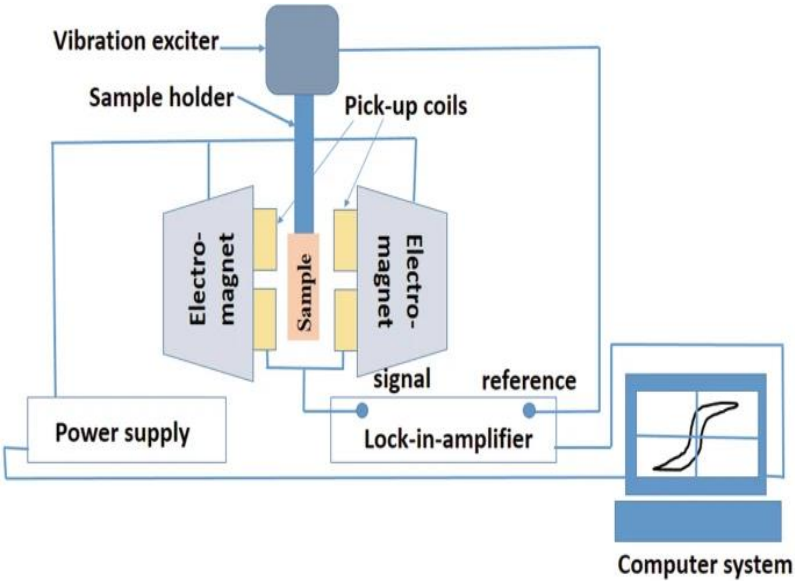

Figure 12. Schematic of a Vibrating Sample Magnetometer (VSM). Generating vibration, inducing voltage, amplifying signals, detecting signals, and collecting and analyzing data. Figure 12 is taken from Ref. [50]

In this study, the VSM option of the PPMS was used (*Figure 13)* to measure the magnetic susceptibility of the orthorhombic and monoclinic polymorph of [^{57}Fe(PM-BiA)2(NCS)2]. The temperature dependence of magnetization for both phases was measured under a constant

magnetic field of μ_B = 500 Oe, within the temperature range 5 K < T < 350 K, using the Field-Cooled Cooling (FCC) and Field-Cooled Warming (FCWM) methods. The measurements were conducted in four cycles at varying temperature rates (5, 2, 1 K min^{-1}) in sweep mode.

Figure 13. The Quantum Design PPMS system in JCNS-2 Lab.

The sample preparation (*Figure 14*) was carried out as follows:

First, an empty plastic sample holder was weighed, with the mass recorded as M_{holder}. Further, a few milligrams of the sample were added to one side of the plastic tube, filling approximately half of the tube. The other side of the tube was inserted and gently rotated to ensure the sample was evenly distributed. After loading the sample, the entire tube was weighted, with the total mass recorded as M_{total}. The difference (M_{total}–M_{holder}) represents the mass of the sample used. The plastic tube was loaded into the brass sample holder, ensuring that the sample was centered approximately at 35 mm and the holder was inserted into the instrument for the magnetic measurement. The weights for the orthorhombic polymorph was 4.0 mg and for the monoclinic polymorph 4.9 mg. The scanning range was centered on the sample, with the offset position set at 36.64 mm and 35.70 mm, respectively.

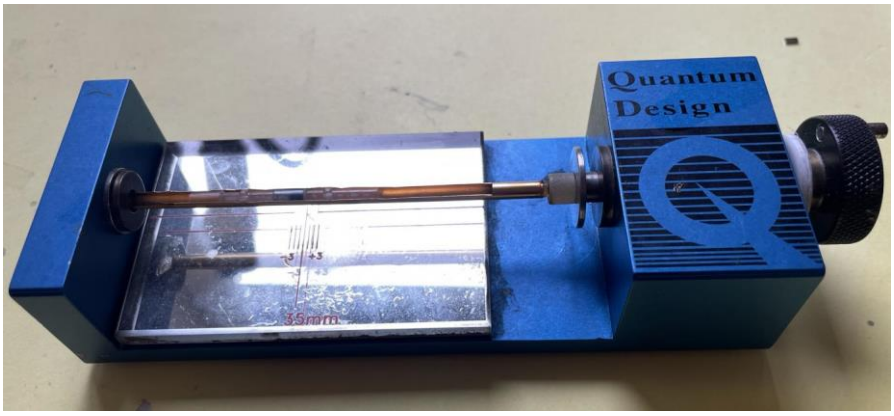

Figure 14. Picture of the VSM sample holder.

2.3 Fourier Transform Infrared Spectroscopy (FT-IR)

FT-IR spectra were acquired using a Bruker Tensor 27 spectrometer (*Figure 15*) equipped with a Liquid Nitrogen-Cooled Mercury Cadmium Telluride Detector (LN-MCTs), operating within a spectral range of 4000 to 200 cm^{-1}. Sample measurements involved 120 scans, while the background was measured with 16 scans.[51] Powdered samples were evenly spread on a Specac Golden Gate diamond window for the measurement. The band intensities were recorded in transmittance. The acquired data were processed to identify characteristic peaks, enabling the determination of the main molecular groups present in the samples through IR spectral analysis.

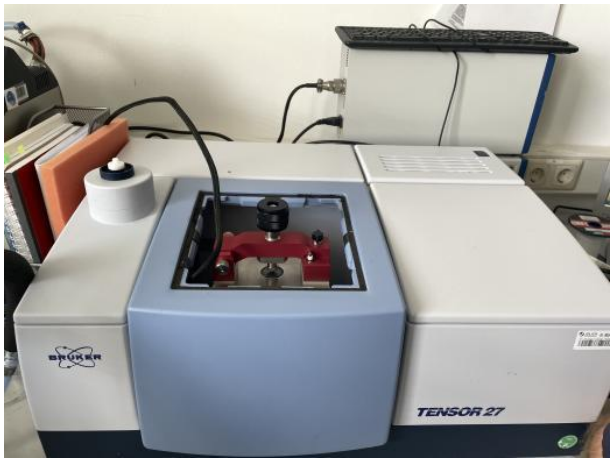

Figure 15. The Bruker Tensor 27 FT-IR spectrometer.

2.4 Nuclear Magnetic Resonance (NMR)

The NMR spectra were recorded using a Bruker Ascend 200SWB spectrometer (600 MHz) operating at room temperature (*Figure 16*). The measurements included ^{1}H NMR and, if applicable, ^{13}C NMR spectra. The acquired data were processed using *MestreNova* software,[52] which involved baseline correction, phase adjustment, and chemical shift referencing. Peaks were integrated, and multiplicities were assigned to identify the structure and confirm the purity of the compound.

For NMR measurement in this study, the sample was prepared by dissolving approximately 10 mg of the compound in 0.6 mL of deuterated solvent, such as $CDCl_3$.The solution was then transferred into a 5 mm NMR tube, with the sample height adjusted to about 6 to 7 cm to ensure optimal detection.

Figure 16. The NMR spectroscopy measurements in this study were performed on a Bruker Ascend 200SWB, operating at 600 MHz.

2.5. Thin Layer Chromatography (TLC)

Thin-layer chromatography (TLC) allows for multiple detection methods of separated components, using UV light or chemical reactions that generate colored spots.[53] The principle of TLC is to separate components in a mixture based on their affinity for the stationary and mobile phases. The stationary phase consists of a thin layer of silica gel on the TLC plate, while the mobile phase is a solvent mixture. After sample application via capillary spotting onto the stationary phase, the mobile phase carries the components up the plate. Components with higher affinity for the mobile phase (solvent) travel faster, while those with greater interaction with the stationary phase move more slowly. This differential movement based on polarity allows for the separation of the mixture into its components.[54] In the experiment, TLC plates with silica gel 60 and a fluorescence indicator (F_{254}) were used.[53]

For the measurements, TLC plates were cut into strips with approximate dimensions 3×8 cm and labeled with a pencil. Using capillary tubes, sample drops were placed along the bottom edge of the TLC plate, with each sample aligned in its own "lane" for upward movement. Different samples were arranged in a row. A solvent mixture of varying polarities was then poured into a glass development chamber to a depth of about 2 cm. The TLC plate was placed along the wall of the chamber, which was then covered. When the solvent front nearly reached the top, the plate was removed from the chamber, and the solvent front was marked with a pencil. After allowing the solvent to evaporate, the plate was placed under a UV lamp (254 nm), where distinct spots appeared at various positions (*Figure 17*).

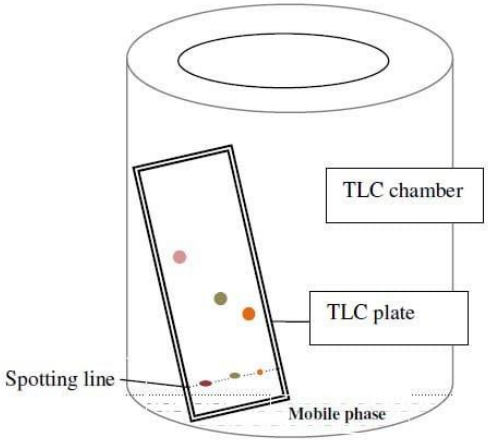

Figure 17. Illustration of TLC setup. Figure 17 is taken from Ref. [55].

3. Materials Synthesis

3.1 General Methods and Reagents

Air- and moisture-sensitive reactions were conducted using a Schlenk line or in a glovebox. The Schlenk line was used to maintain an inert atmosphere of argon for reactions requiring strictly anaerobic and anhydrous conditions. Standard techniques, including vacuum and nitrogen/argon purge cycles, were applied to degas solvents and remove residual moisture.

An oil bath was used for heating to ensure even heat distribution and maintain a stable reaction temperature. The temperature of the oil bath was monitored with a thermocouple. For low-temperature experiments, a liquid nitrogen cooling system was employed. Liquid nitrogen cooling was typically used for rapid cooling or to maintain a low-temperature environment. Additionally, recrystallization was performed by storing samples in a freezer at -26 °C to promote crystal formation and purification.

For reagents and reactions that required complete isolation from atmospheric contaminants, a glovebox (maintained with high-purity argon) was used. The glovebox was equipped with a refrigerator for storage of highly sensitive materials, ensuring stable and controlled conditions for sensitive reagents such as pyridine-2-carboxyaldehyde.

Detailed information on the chemical reagents used in this study is provided in *Section 6.3*. Specific reactants requiring special handling are described within the experimental procedures.

3.2 Synthesis of PM-BiA Ligand: N-(2'-pyridylmethylene)-4-aminobiphenyl

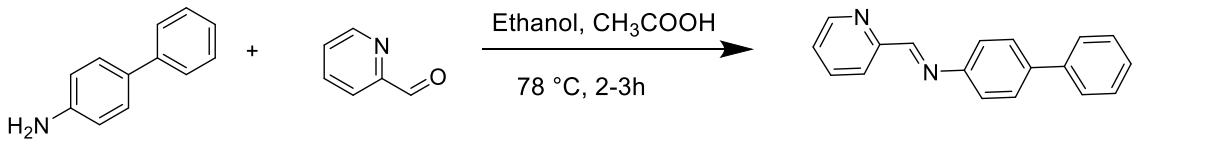

4-aminobiphenyl
$C_{12}H_{11}N$
Molecular Weight: 169 g/mol

pyridine-2-carboxyaldehyde
C_6H_5NO
Molecular Weight: 107 g/mol

N-(2'-pyridylmethylene)-4-aminobiphenyl
$C_{18}H_{14}N_2$
Molecular Weight: 258 g/mol

Figure 18. Reaction formula for the synthesis of N-(2'-pyridylmethylene)-4-aminobiphenyl.

4-Aminobiphenyl (3.39 g, 20 mmol) and pyridine-2-carboxyaldehyde (3.23 g, 31 mmol) were added to a round-bottom flask. 300 mL of ethanol was and subsequently. Then, 3-4 drops of acetic acid were added to the mixture. The reactants were heated in a silicon oil bath under reflux at 86 °C, under stirring for 2 hours. Afterwards, the oil bath was removed, and the mixture was cooled down to room temperature. Ethanol was then removed with a rotary evaporator while gradually reducing the pressure from 350 to 0 mbar to avoid boiling of the liquid. Upon obtaining a light brown solid in the flask, diethyl ether was added to the mixture to dissolve the solid completely. The mixture was stirred and heated in an oil bath at 40°C until the solid was completely dissolved. The oil bath was then removed, and the mixture was refrigerated for recrystallization. After recrystallizing for one day at around -30°C from dimethyl ether, a golden

yellow powder formed N-(2'-pyridylmethylene)-4-aminobiphenyl ligand was obtained.[56] Yield: 2.37 g, 9.18 mmol, 45.8%. ^{1}H NMR: (600 MHz, $CDCl_3$) δ [ppm] = 7.30–7.25 (2H, m), 7.34–7.30 (2H, m), 7.38 (2H, t, *J* = 7.7 Hz), 7.57–7.54 (2H, m), 7.59 (2H, d, *J* = 8.4 Hz), 7.76 (1H, td, *J* = 7.7, 1.7 Hz), 8.18–8.12 (1H, m), 8.61 (1H, s), 8.66 (1H, d, *J* = 4.9 Hz).

3.3. Synthesis of $^{57}FeSO_4 \cdot 7H_2O$

$$^{57}Fe + H_2SO_4 + 7H_2O \xrightarrow{\text{60-70 °C, 2-3 days}} {}^{57}FeSO_4 \bullet 7H_2O + H_2$$

Figure 19. Reaction formula for the synthesis of $^{57}FeSO_4 \cdot 7H_2O$.

The used ^{57}Fe sample was enriched to 96.06% isotopic purity (Isoflex, San Francisco, USA). Weighted bulk ^{57}Fe (0.101 g, 1.77 mmol, 1 eq.) was placed in a Schlenk line flask. Under argon, the metal was mixed with of 1 M sulfuric acid (2.63 mL, 1.47 eq.) and stirred under argon while being heated at 60 to 70°C for 2 to 3 days until the iron was completely dissolved, forming a pale blue solution. After removing the oil bath and cooling, solid sodium bicarbonate (0.139 g, 1.65 mmol) was added to neutralize the solution to a final concentration of 1 M. After the addition of sodium bicarbonate, the liquid turned yellow. The mixture was rapidly frozen in liquid nitrogen, followed by overnight freeze-drying under vacuum to remove the water. The product obtained was a mixture of sodium sulfate and iron(II) sulfate heptahydrate, which appeared as a white-pale blue powder.[57] The yield of $^{57}FeSO_4 \cdot 7H_2O$ was reported in *Table 1*.

Table 1. Preparation attempts of $^{57}FeSO_4 \cdot 7H_2O$ from elementary ^{57}Fe metal.

Entry	Amount of ^{57}Fe (g)	Reaction-Time (day)	Temperature (℃)	Condition	Solution colour	Yield %
1	0.098	4	60	Vacuum-filled and sealed with argon	Pale yellow	0
2	0.101	3	70	Vacuum-filled and sealed with argon.	Pale blue	55.9
3	0.096	4	68	Vacuum-filled and sealed with argon.	Pale yellow	0
4	0.099	2	70	Continuously Argon	Pale blue	56.5

3.4 Optimization of the Synthesis Conditions for SCO Complex $[^{57}Fe(PM\text{-}BiA)_2(NCS)_2]$

In this study, $^{nat}FeSO_4 \cdot 7H_2O$ was utilized to replicate the procedure outlined in *Section 3.5.* The reaction temperature for the PM-BiA ligand with $Fe(NCS)_2$ was systematically varied to investigate its effect on the reaction outcome. The resulting products and their yields at each temperature condition are summarized in *Table 2*. This analysis provides insights into the

optimal conditions for maximizing yield and determining any notable variations in product formation across the tested temperatures.

Table 2. Synthesis attempts of $[Fe(PM\text{-}BiA)_2(NCS)_2]$.

Entry	Time (h)	Temperature (°C)	Color	Phase	Yield (%)
1	1	25	Dark green	Monoclinic	67.5
2	1	50	Black	Orthorhombic	81.4
3	1	70	Black	Orthorhombic	63.9

Based on the data presented in *Table 2,* it is evident that the reaction temperature significantly influences the phase of the resulting product. This result suggests that 50°C is the optimal temperature for maximizing orthorhombic-selective production. Adjusting the reaction temperature allows control over the phase of the product, making it possible to refine the product composition by changing the thermal conditions.

From these observations, 50°C was chosen as the ideal temperature in *Section 3.5* to achieve the highest yield of the orthorhombic phase of $[^{57}Fe(PM\text{-}BiA)_2(NCS)_2]$, while the monoclinic phase was obtained with the highest yield at room temperature (without heating).

3.5 Synthesis of SCO Complex $[^{57}Fe(PM\text{-}BiA)_2(NCS)_2]$

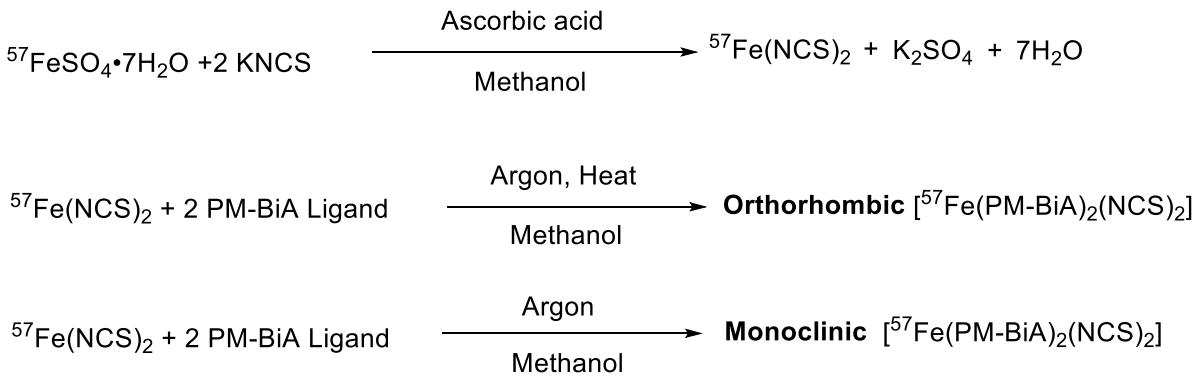

Figure 20. Reaction formula for the synthesis of $^{57}Fe(NCS)_2$ and two polymorphs of $[^{57}Fe(PM\text{-}BiA)_2(NCS)_2]$.

The synthesis was conducted under argon atmosphere to avoid the oxidation of iron. In a Schlenk flask, iron(II)-57 sulfate heptahydrate $^{57}FeSO_4{\cdot}7H_2O$ (1.42 mmol, 0.278 g, 1 eq.), potassium thiocyanate (2.90 mmol, 0.282 g, 2 eq.), were added. A spatula of ascorbic acid was added to prevent the oxidation of iron(II). The mixture was dissolved in 15 mL of methanol and stirred until the solution became a white suspension, indicating the formation of $^{57}Fe(NCS)_2$.The white suspension was then carefully filtered through celite to obtain a clear solution of $^{57}Fe(NCS)_2$.The celite was washed with 2 × 5 mL of methanol, to ensure that all of the product was filtered off.

The PM-BiA ligand (2.87 mmol, 0.742 g, 2 eq.) was dissolved in another Schlenk flask in 30 mL of methanol and the resulting mixture was stirred in oil bath at 50°C.

- For the synthesis of the orthorhombic polymorph, the $^{57}Fe(NCS)_2$ solution was drawn up with a syringe and added dropwise to the ligand solution. It was then heated and stirred in an oil bath at 50°C for 2 hours, resulting in the precipitation of the product from the solution.The filtered orthorhombic polymorph was in black powder (*Figure 21a*) and washed with methanol and diethyl ether successively. The final product was dried in air. The yield of black orthorhombic [$^{57}Fe(PM\text{-}BiA)_2(NCS)_2$] solid was 0.35 g (0.455 mmol, 45.5%).
- For synthesizing the monoclinic polymorph, the ligand was dissolved in 30 mL of methanol, and the resulting mixture was stirred without heating, which is the distinguishing factor in the synthesis of the two phases. [56] The filtered monoclinic polymorph was in dark green (*Figure 21b*) and treated with exactly the same procedure. The yield of the dark green monoclinic [$^{57}Fe(PM\text{-}BiA)_2(NCS)_2$] solid was 0.40 g (0.52 mmol, 36.7%).

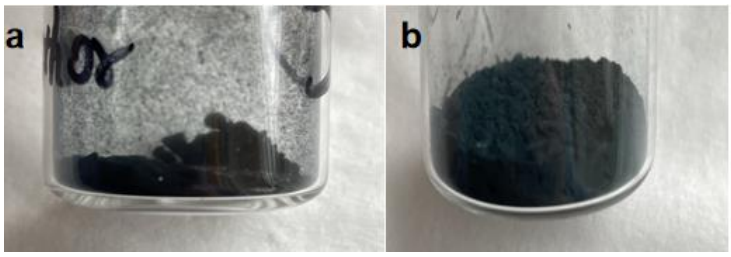

Figure 21. (a) Orthorhombic polymorph of [$^{57}Fe(PM\text{-}BiA)_2(NCS)_2$] with a black color. (b) Monoclinic polymorph of [$^{57}Fe(PM\text{-}BiA)_2(NCS)_2$] with a dark green color.

Table 3. Reactants used for the preparation of the orthorhombic and monoclinic phases of [$^{57}Fe(PM\text{-}BiA)_2(NCS)_2$].

Phase	Reactant (g)	Amount (g)	Amount (mmol)
Monoclinic	$^{57}FeSO_4{\cdot}7H_2O$	0.281	1.01
	KNCS	0.236	2.43
	PM-BiA ligand	0.516	2.00
Orthorhombic	$^{57}FeSO_4{\cdot}7H_2O$	0.278	1.00
	KNCS	0.282	2.90
	PM-BiA Ligand	0.742	2.87

3.6 Synthesis of Catalyst $[NH_4]_3[CrMo_6O_{18}(OH)_6]\cdot 7H_2O$ for Catalytic Oxidation

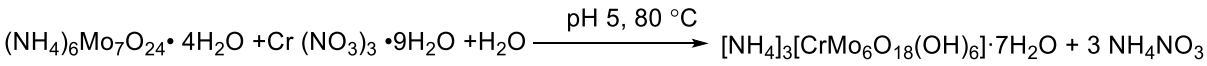

Figure 22. Reaction formula for the synthesis of $[NH_4]_3[CrMo_6O_{18}(OH)_6]\cdot 7H_2O$.

The $(NH_4)_6Mo_7O_{24}\cdot 4H_2O$ (2.498 g, 2 mmol) was dissolved in 20 mL of distilled water and stirred in an oil bath at 80°C. $Cr(NO_3)_3\cdot 9H_2O$ (1.149 g, 2.875 mmol) was dissolved in 10 mL of distilled water and added dropwise to the above solution using a dropping funnel. During the dropwise addition, the pH of the mixture was frequently measured and maintained around 5. The color of the solution gradually changed from light pink to burgundy. After the dropwise addition was complete, the mixture was stirred at 80°C.After 1 hour, the hot solution was filtered, and the filtrate was poured into a Petri dish, wrapped in an aluminum foil to prevent complete evaporation at room temperature. After 2 days, burgundy crystals were collected by vacuum filtration and recrystallized from water. The recrystallized purple-pink powder was vacuum-dried overnight. The final product, $[NH_4]_3[CrMo_6O_{18}(OH)_6]\cdot 7H_2O$ 1 is shown in *Figure 23b*, was obtained. [58] Yield: 0.928 g, 0.793 mmol, 39.7 % Ref: 95%[59]. FT-IR: 3157.0 cm^{-1} (vas NH, weak), 1636.5 cm^{-1} (δ OH, weak), 1399.3 cm^{-1} (δ NH, weak),936.6 cm^{-1} (v Mo=O, medium), 887.4 cm^{-1} (v Mo=O, s), 634.8 cm^{-1} (v Mo-O-Mo, vs).

Figure 23. The structural formula (a) and the appearance of the powder of $[NH_4]_3[CrMo_6O_{18}(OH)_6]\cdot 7H_2O$ 1 (b). Figure 23a is taken from Ref. [59].

3.7 Catalytic Oxidation of 2-Pyridinecarboxaldehyde from 2-Picoline

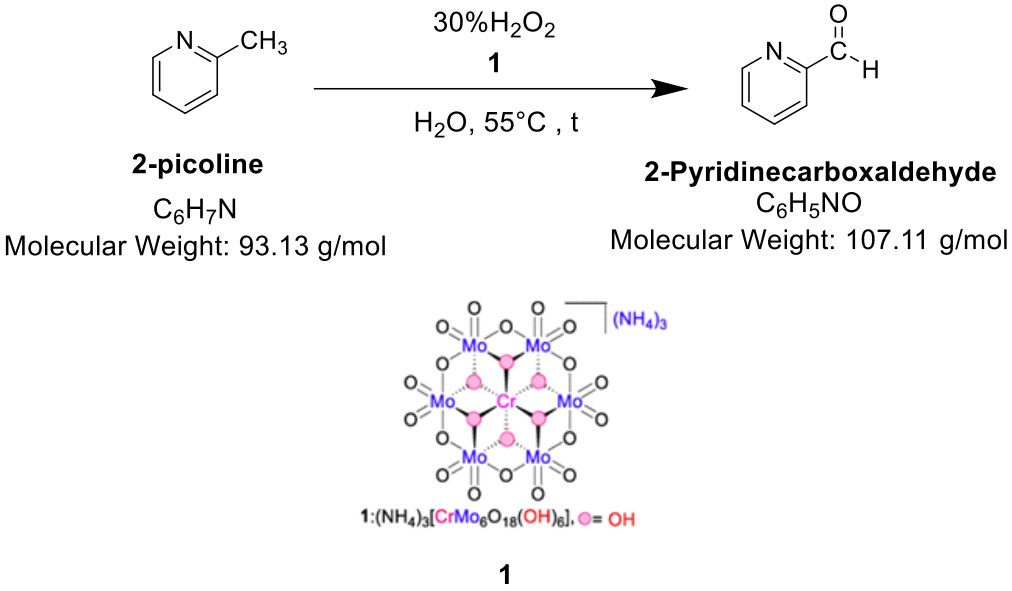

Figure 24. Reaction formula of the catalytic oxidation of 2-pyridinecarboxaldehyde from 2-picoline.

2-picoline (1 eq., 10.7 mmol, 1.069 g) and catalyst **1** (1.0 mol%, 0.156 g) were added into water, resulting in an immediate color change to green. Subsequently, 30% H_2O_2 (2 eq., 21.4 mmol, 2.2 mL) was added dropwise via a syringe, causing the solution to rapidly change to a brown-wine color. The reaction mixture was then heated in an oil bath at 55 °C. Upon heating, the solution quickly turned yellow, and the reaction continued for 18 hours. Afterwards, the mixture was cooled to room temperature and tested by TLC (Ethyl acetate: hexane = 1:1). [60] Since TLC indicates no conversion to target molecule in reaction mixture, no further purification was carried out.

4. Results and Discussion

4.1 The Synthesis Results and Reaction Mechanism of the PM-BIA Ligand

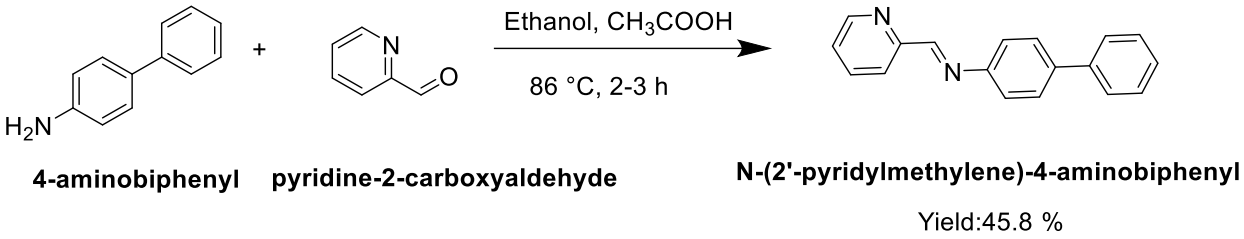

Figure 25. Reaction formula for the synthesis of PM-BiA Ligand and yield of the product.

The experimental ^{1}H-NMR data was in good agreement with the literature values, indicating that the target compound was successfully synthesized.[56] Additionally, minor solvent peaks for methanol and diethyl ether were observed in the spectrum, consistent with experimental expectations.[62]

The yield was not reported in the literature; based on experimental results, the low yield could be attributed to the formation of water as a byproduct during the synthesis of the Schiff base. Water promoted the hydrolysis of the imine, shifting the equilibrium back toward the starting materials and thereby reducing the overall yield.[63] The use of recrystallization to purify the product led to a loss in yield, as some of the product remained dissolved in the mother liquor. Additionally, the primary amine used as an adduct was biphenyl amine, which exhibited lower nucleophilicity due to the conjugation effect, further contributing to the reduced yield. [64]

For mechanism consideration (*Figure 26*), firstly, the nitrogen atom of the amino group in 4-aminobiphenyl acted as a nucleophile and attacked the carbonyl of 2-picoline, forming intermediate **2** under acidic conditions. The lone pair on the nitrogen atom of the 4-aminobiphenyl abstracted a proton from the -NH_2^+- group in intermediate **2**. After the proton transfer, a carbinolamine was formed, which served as a crucial intermediate for the subsequent dehydration to form the Schiff base. The carbinolamine underwent protonation under acidic conditions, making the -OH group a better leaving group, leading to the formation of intermediate **3**. The elimination of a water molecule then occurred, resulting in an iminium ion **4**, where the nitrogen atom carried a positive charge, making the iminium ion unstable. With deprotonation of the iminium ion, the Schiff base product, N-(2'-pyridylmethylene)-4-aminobiphenyl, was formed . [60,61]

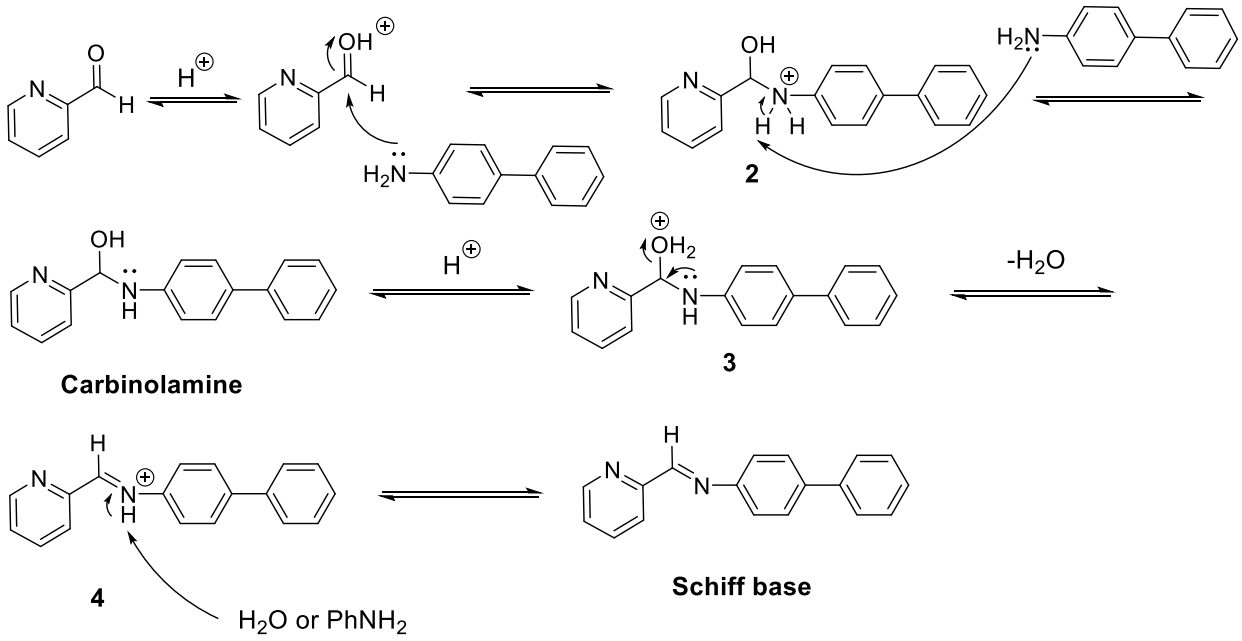

Figure 26. Mechanism of the Reaction between 4-Aminobiphenyl and Pyridine-2-carboxylaldehyde.

4.2 Structure Analysis of SCO Complex

4.2.1 Le Bail Refinement

To determine the lattice parameters of the two polymorphs, monoclinic and orthorhombic, of [^{57}Fe(PM-BiA)$_2$(NCS)$_2$], the PXRD data mentioned in *Section 2.1* was used. The measured data were subjected to Le Bail refinement using the software *JANA2006*. The main objective of the Le Bail refinement [66] *(Figure 27)* is to fit the experimental diffraction pattern without requiring a structural model by optimizing the unit cell parameters, background, and peak shape parameters to minimize the difference between the observed intensities (I_{obs}) and the calculated intensities (I_{cal}) as much as possible. The main steps of the Le Bail refinement are as follows:

- Initial Model Setup: Begin by providing the initial lattice parameters (e.g., unit cell parameters *a*, *b*, *c*, and angles *α*, *β*, *γ*), space group information (*Pccn*, *P*2$_1$*/c)*, the type of measurement instrument such as X-ray or neutron diffraction, and the appropriate wavelength. The measurement temperature should be input, and the suitable 2*θ* range from the diffraction pattern should be manually selected for fitting. The background parameters are set using Legendre polynomials.
- Selection of Peak Shape Function: Choose an appropriate peak shape model (e.g., Gaussian, Lorentzian, or Pseudo-Voigt function) to adjust the diffraction peak shapes. Initial settings for peak width, shape, and symmetry can be made.

- Zero Shift Adjustment: The software *JANA2006* will automatically adjust this parameter to correct the position shifts of the diffraction peaks caused by instrument calibration errors.
- Asymmetry parameters: The Asymmetry parameters are used to correct the asymmetry of diffraction peaks. At low angle range, peak asymmetry is caused by optical system or sample effects. At low 2θ angles, Parameters like *HpS/L* or *HmS/L* are adjusted to optimize the asymmetry correction, allowing the experimental data to be better matched with theoretical peak shapes for more accurate refinement results.
- Iterative Refinement Process: The software iteratively adjusts the parameters, optimizing the fit between the calculated and observed diffraction patterns.
- Output Results and Plotting: After completing the refinement, the software outputs quality indicators *R* of the fit, such as the profile fitting error (*R*p) and the weighted profile fitting error (*R*wp). The refined files, specifically the *PICS RULES* file, can be processed using *Origin 2024* to generate the XRD pattern.

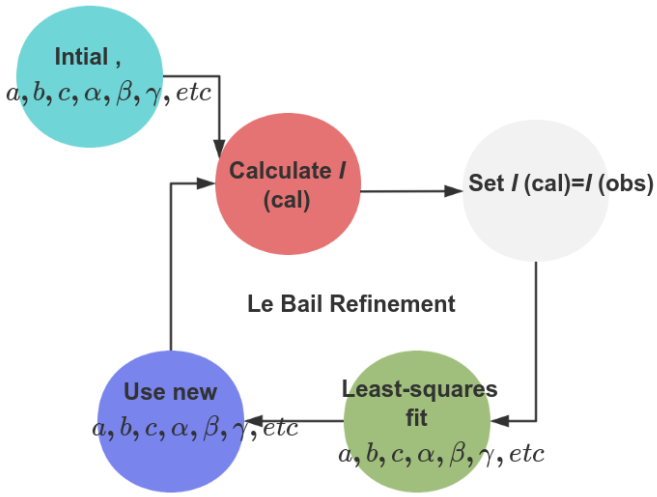

Figure 27. The Le Bail refinement process is shown in the flow diagram.

4.2.2 Structural analysis of [^{57}Fe(PM-BiA)$_2$(NCS)$_2$] and [Fe(PM-BiA)$_2$(NCS)$_2$]

The crystal structures of the two polymorphs of [^{57}Fe(PM-BiA)$_2$(NCS)$_2$] were determined directly from PXRD data. The monoclinic phase of [^{57}Fe(PM-BiA)$_2$(NCS)$_2$] was analyzed using the Le Bail fitting method with data from two PXRD experiments using two different devices (STOE or xHuber), yielding refinement results shown in *Figure 28.* The final fitting parameters indicated a GOF of 0.77, an *R*wp of 1.82%, and an *R*p of 2.27 % (STOE); a GOF of 6.95, an *R*wp of 1.11%, and an *R*p of 1.63% (xHuber).

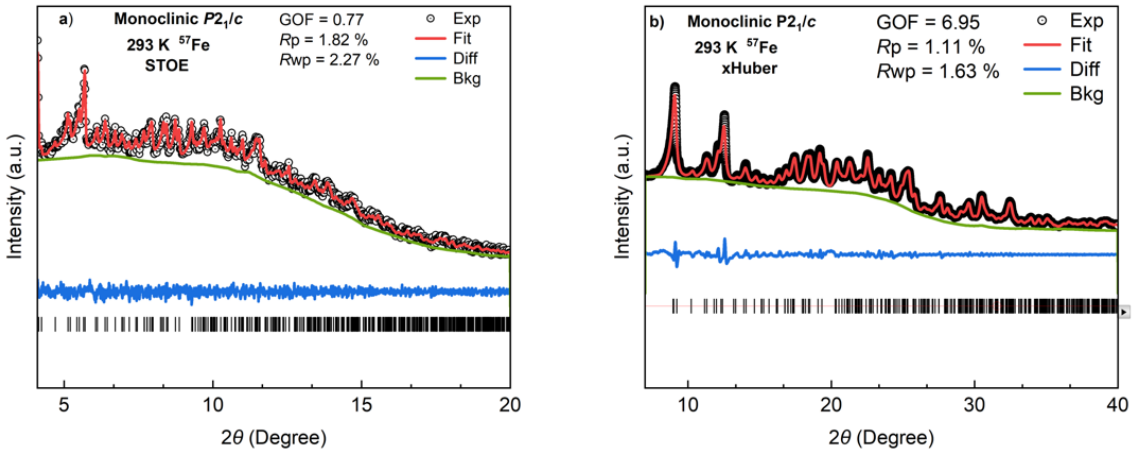

Figure 28. The Le Bail refinement of the PXRD patterns for the monoclinic polymorph of [^{57}Fe(PM-BiA)$_2$(NCS)$_2$] obtained by (a) STOE data and (b) xHuber diffractometers at room temperature, respectively. (black circle: experimental data; red line: calculated data; green line: background; tick marks: peak positions; blue line: difference plot = $I_{obs} - I_{calc}$).

Figure 28a and *b* shows the XRD pattern of monoclinic [^{57}Fe(PM-BiA)$_2$(NCS)$_2$] obtained by STOE and xHuber diffractometer, respectively. Due to excessive noise in *Figure 28a*, the data obtained by the STOE only provides limited reliability for refinement. In contrast, according to the refinements shown in *Figure 28b*, it confirms that the monoclinic phase of [^{57}Fe(PM-BiA)$_2$(NCS)$_2$] is nearly pure.

The XRD patterns of the orthorhombic phase of [^{57}Fe(PM-BiA)$_2$(NCS)$_2$] have also been obtained by two different devices (STOE or xHuber), the refinement of both patterns can be found in *Figure 29.* The final fitting parameters indicated a GOF of 1.60, an *R*wp of 3.02 %, and an *R*p of 4.09 % (STOE); a GOF of 7.03, an *R*wp of 1.11%, and an *R*p of 1.52% (xHuber).

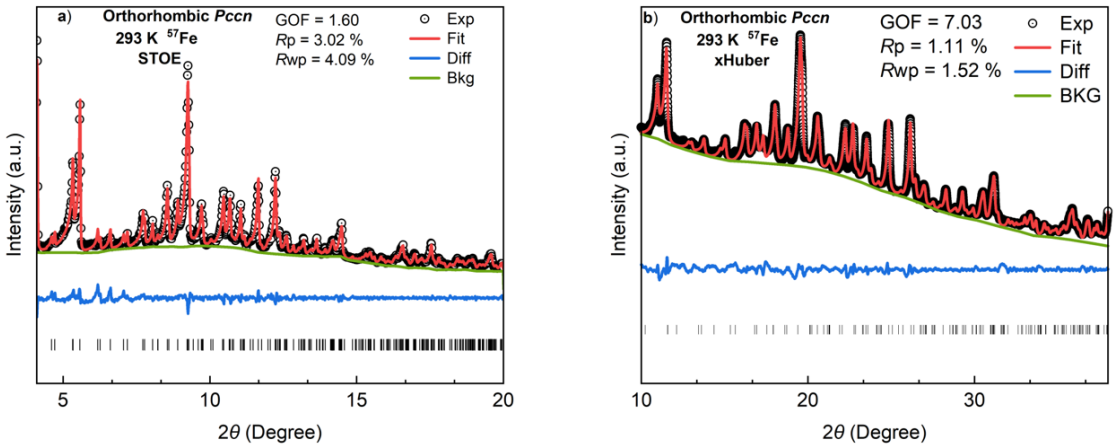

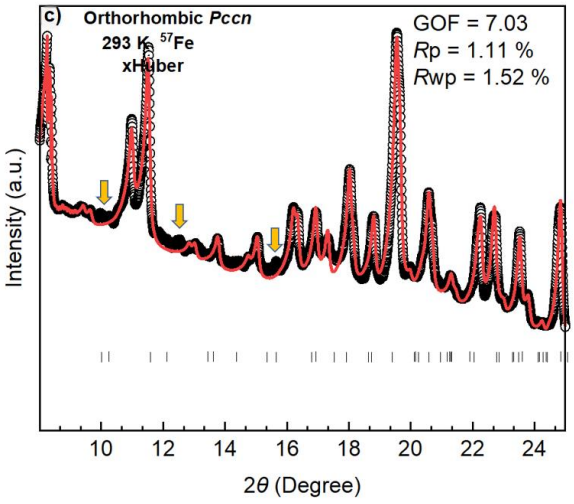

Figure 29. The Le Bail refinement of PXRD patterns for the monoclinic polymorph of [^{57}Fe(PM-BiA)$_2$(NCS)$_2$] by (a) STOE and (b) xHuber diffractometers at room temperature respectively. (c) zoom-in XRD patterns from (b), the impurity peaks are marked by yellow arrows. (Black circles: experimental data; red line: calculated data; green line: background; tick marks: peak positions; blue line: difference plot = $I_{obs} - I_{calc}$).

According to the refined patterns displayed in *Figure 29a* and *b*, it also confirms that the orthorhombic phase of the [^{57}Fe(PM-BiA)$_2$(NCS)$_2$] has been successfully synthesized. However, when we check the data in detail, few extra peaks can be found in the pattern, as displayed in *Figure 29 c and d*. It evidences that the phase of orthorhombic [^{57}Fe(PM-BiA)$_2$(NCS)$_2$] is not pure. In *Figure 29c*, three impurity peaks are observed. When comparing their 2θ positions with those in *Figure 28b*, the peaks at 2θ = 10.26° and 15.65° correspond to the monoclinic polymorph of the [^{57}Fe(PM-BiA)$_2$(NCS)$_2$]. However, the peak at 2θ = 12.545° does not match any expected reflections for the monoclinic phase and might belong to other impurities.

Table 4a provides unit cell parameters obtained from the refinement of the XRD patterns for both polymorphs of [^{57}Fe(PM-BiA)$_2$(NCS)$_2$] at 293 K. Additionally, a comparison was made between the unit cell parameters of [^{57}Fe(PM-BiA)$_2$(NCS)$_2$] and those reported in the literature for [Fe(PM-BiA)$_2$(NCS)$_2$].[67] In terms of the data quality, only the data obtained by xhuber diffractometer will be used for comparison.

- Monoclinic Polymorph:

The lattice parameters (*a*, *b*, *c*) and unit cell volume (*V*) of [^{57}Fe(PM-BiA)$_2$(NCS)$_2$], measured by both xHuber and STOE, agree with the values reported in the literature when compared to [Fe(PM-BiA)$_2$(NCS)$_2$]. [67]

- Orthorhombic Polymorph:

The lattice parameters (*a*, *b*, *c*) and unit cell volumes (*V*) of [^{57}Fe(PM-BiA)$_2$(NCS)$_2$] measured by xHuber (0.895%) and STOE (0.722%) are above those reported in the literature when compared to [Fe(PM-BiA)$_2$(NCS)$_2$]. [67]

Table 4. Crystal data for the two polymorphs of [^{57}Fe(PM-BiA)$_2$(NCS)$_2$] with a comparison to the reference data of [Fe(PM-BiA)$_2$(NCS)$_2$] .[67]

	Monoclinic 293 K		Orthorhombic 293 K		Monoclinic (Ref.)[67] 293 K	Ortho-rhombic (Ref.)[67] 293 K
Chemical Formula	$^{57}FeN_6S_2C_{38}H_{28}$		$^{57}FeN_6S_2C_{38}H_{28}$		$FeN_6S_2C_{38}H_{28}$	
Space group	*P*2$_1$/*c*		*Pccn*		*P*2$_1$/*c*	*Pccn*
a (Å)	17.571(11)	17.578(6)	12.990(3)	12.984(4)	17.570(5)	12.949(7)
b (Å)	12.601(9)	12.608(5)	15.243(3)	15.226(3)	12.602(5)	15.183(2)
c (Å)	17.329(10)	17.332(5)	17.641(4)	17.638(4)	17.358(5)	17.609(5)
β (°)	115.595(39)	115.584(20)	90.000	90.000	115.68(1)	90.000
V (Å^3)	3460 (5)	3465(3)	3493(1)	3487(2)	3464(2)	3462(2)
Radiation	Cu K_α	Mo K_α	Cu K_α	Mo K_α	Mo K_α	Mo K_α
Device	xHuber	STOE	xHuber	STOE	*κ* CCD	*κ* CCD

As shown in Table 4, comparing the all the lattice parameters from the refinement of ^{57}Fe compounds and the data from reference, nearly all the parameters are similar with each other, indicating the substitution with ^{57}Fe only induced minor changes in lattice parameters and cell volume.

In *Section 3.4*, products with different phases were synthesized by adjusting the temperature, and their phases were identified using PXRD analysis.

The monoclinic phase of [Fe(PM-BiA)$_2$(NCS)$_2$] was analyzed using the Le Bail fitting method with data from two PXRD experiments using two different devices (STOE or xHuber), yielding refinement results shown in *Figure 30.* The final fitting parameters indicated a GOF of 0.87, an *R*wp of 2.96%, and an *R*p of 3.74 % (STOE); a GOF of 6.79, an *R*wp of 1.25%, and an *R*p of 1.74 % (xHuber).

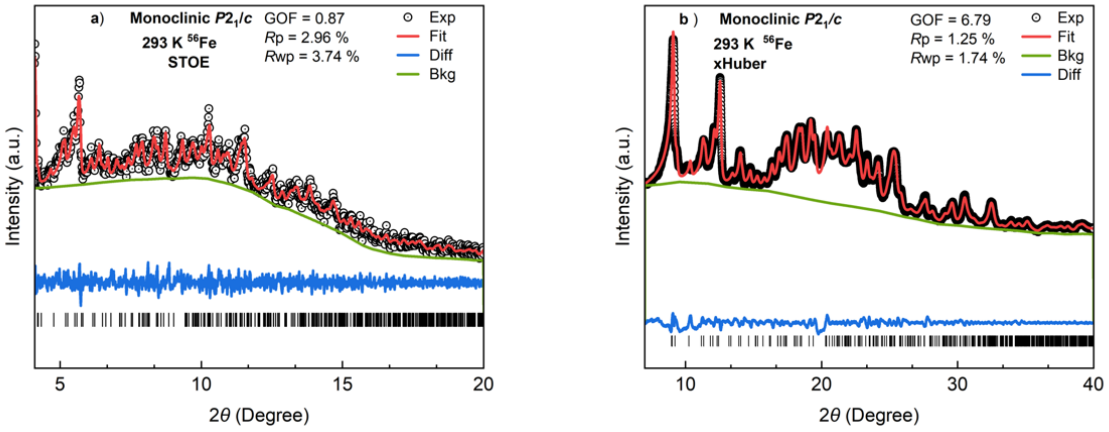

Figure 30. The Le Bail refinement of PXRD patterns for the monoclinic polymorph of [Fe(PM-BiA)$_2$(NCS)$_2$] by (a) STOE and (b) xHuber diffractometers at room temperature respectively. (Black circle: experimental data; red line: calculated data; green line: background; tick marks: peak positions; blue line: difference plot = $I_{obs} - I_{calc}$).

A comparison between *Figure 30a* and *Figure 30b* shows that the data from STOE is less reliable than that from xHuber due to excessive noise. Analysis of *Figure 29b* shows no significant impurity peaks. However, given the refinement results and the data quality, there might be some uncertainties. Overall, the synthesized monoclinic phase of [Fe(PM-BiA)$_2$(NCS)$_2$] appears to be relatively pure.

The orthorhombic phase of [Fe(PM-BiA)$_2$(NCS)$_2$] was analyzed using the Le Bail fitting method with data from two PXRD experiments using two different devices (STOE or xHuber), yielding refinement results shown in *Figure 30.* The final fitting parameters indicated a GOF of 3.53, *R*wp of 2.96%, and an *R*p of 3.74 % (STOE); a GOF of 6.79, an *R*wp of 1.25%, and an *R*p of 1.74 % (xHuber).

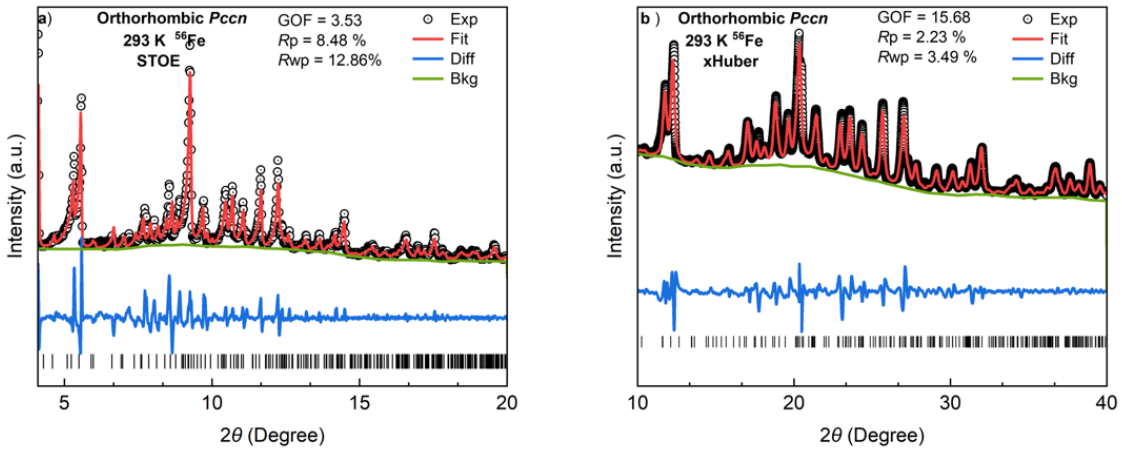

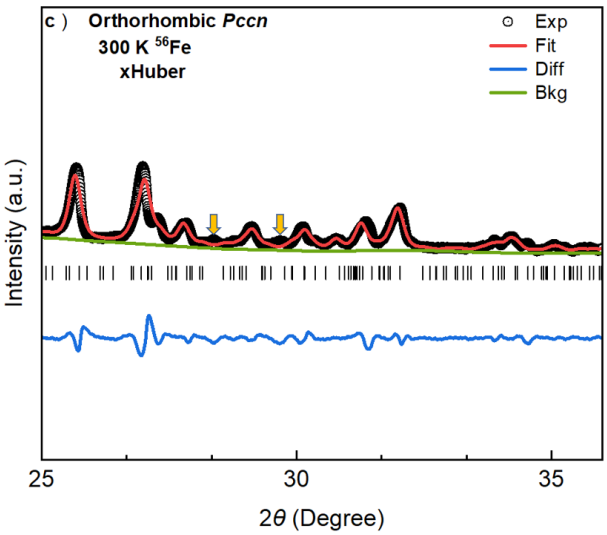

Figure 31. The Le Bail refinement of PXRD patterns for the monoclinic polymorph of [Fe(PM-BiA)$_2$(NCS)$_2$] by (a) STOE and (b) xHuber diffractometers at room temperature respectively. (c) zoom-in XRD patterns from (b).(black circle: experimental data; red line: calculated data; green line: background; tick marks: peak positions; blue line: difference plot = $I_{obs} - I_{calc}$).

Similarly, there is too much noise in the pattern obtained by STOE, as shown in *Figure 31a*. According to the refined pattern shown in *Figure 31b*, it confirms that the orthorhombic polymorph has been synthesized and the phase is not completely pure. In *Figure 31c*, two obvious impurity peaks are observed at 2θ = 28.37° and 29.67°. When compared with *Figure 30b*, these peaks are likely attributed to the monoclinic phase.

Based on the crystal data provided in *Table 5,* the phases of products synthesized under different conditions for the monoclinic and orthorhombic polymorphs of [Fe(PM-BiA)$_2$(NCS)$_2$] were analyzed and compared with reference data.[67] Additionally, considering the data quality, only the data obtained by xhuber diffractometer will be used for comparison.

- Monoclinic polymorph:

The lattice parameters(*a*, *b*, *c*) and unit cell volumes (*V*) of [Fe(PM-BiA)$_2$(NCS)$_2$], measured by both xHuber and STOE, show slight deviations from the values reported in the literature. The lattice parameters data from both instruments are slightly smaller compared to the literature. The unit cell volume (*V*) deviations are: xHuber (−0.61%).

For the monoclinic phase,

- Orthorhombic polymorph:

The lattice parameters (*a*, *b*, *c*) and unit cell volumes (*V*) of [Fe(PM-BiA)$_2$(NCS)$_2$], measured by xHuber and STOE, show slight deviations from the values reported in the literature. The lattice parameters are generally slightly larger than the literature values, except for *b* measured by STOE, which is slightly smaller. The unit cell volumes (*V*) from both instruments are also slightly larger, with deviations of xHuber (3.21%).

Table 5. Crystal data for the two polymorphs of $[Fe(PM\text{-}BiA)_2(NCS)_2]$ with a comparison to the reference data of $[Fe(PM\text{-}BiA)_2(NCS)_2]$.[67]

	Monoclinic 293 K		Orthorhombic 293 K		Monoclinic (Ref.)[67] 293 K	Orthorhombic (Ref.)[67] 293 K
Chemical Formula	$FeN_6S_2C_{38}H_{28}$					
Space group	*P*2$_1$/*c*		*Pccn*		*P*2$_1$/*c*	*Pccn*
a (Å)	17.536(13)	17.324(8)	13.058(1)	14.801(8)	17.570(5)	12.949(7)
b (Å)	12.581 (11)	12.293(6)	15.248(1)	13.602(12)	12.602(5)	15.183(2)
c (Å)	17.293 (12)	17.072(8)	17.890(2)	18.935(12)	17.358(5)	17.609(5)
β (°)	115.521 (43)	115.359(35)	90.000	90.000	115.68(1)	90.000
V (Å^3)	3443 (6)	3285(2)	3573(1)	3812(5)	3464(2)	3462(2)
Radiation	Cu K_α	Mo K_α	Cu K_α	Mo K_α	Mo K_α	Mo K_α
Device	xHuber	STOE	xHuber	STOE	*κ* CCD	*κ* CCD

4.3 Magnetism of the SCO Compounds

4.3.1 Data Correction of the Magnetization Data

The magnetization data were measured by the PPMS instrument described in *Section 2.2* During the heating and cooling cycle, $[^{57}Fe(PM\text{-}BiA)_2(NCS)_2]$ undergoes a transition from high-spin (HS) to low-spin (LS) states. In the HS state, the presence of unpaired electrons leads to paramagnetic contributions, as described in *Section 1.5* An example of raw magnetization data as a function of temperature is shown (*Figure 32*), shows an example of raw magnetization data as a function of temperature, divided into three regions: 230 K - 350 K corresponds to the HS-state dominated region, 100 K to 230 K represents the HS-LS transition range.

The region from 5 K to 100 K is where the magnetic moment decreases as the temperature increases. As the temperature increases, the paramagnetic susceptibility decreases, following Curie's law (*Formula 5)*. This suggests that a little amount of sample remains HS state, indicating incomplete spin transition and contributing to the paramagnetic behavior.

The measured magnetic susceptibility often requires correction for underlying diamagnetic effects. [35] Pascal's constants are used to estimate the diamagnetic correction.[68]

In addition to the diamagnetic contribution from the LS state, the plastic sample holder also has diamagnetic contributions. This correction ensures a more accurate representation of the magnetic behavior during the HS-LS transition in the SCO material.

The total measured magnetic susceptibility $\chi_{meas.}$ includes both paramagnetic $\chi_{para.}$ and diamagnetic $\chi_{dia.}$ contributions, which can be calculated was expressed as follows:[10]

$$\chi_{meas.} = \chi_{para.} + \chi_{dia.} \tag{7}$$

As shown in *Figure 32*, two correction regions were selected, labeled as region 1 and region 2, and were fitted independently. The fitting equation is as follows:[10]

$$\chi_{meas.1} = \frac{A_1}{T} + B \tag{8}$$

$$\chi_{meas.2} = \frac{A_2}{T} + B \tag{9}$$

A represents the paramagnetic contribution, B represents diamagnetic contributions from the plastic sample holder.

In the HS region, the proportion of HS state is higher, resulting in a larger paramagnetic contribution. Consequently, A_2 is significantly greater than A_1, where the paramagnetic contribution in region 1 comes only from a small amount of residual HS state $^{57}Fe^{2+}$.[10]

The corrected magnetic moment $\chi_{corr.}$ can be calculated using the following equation, with A_1 chosen for the correction:[11]

$$\chi_{corr.} = \chi_{meas.} - \left(\frac{A_1}{T} + B\right) \tag{10}$$

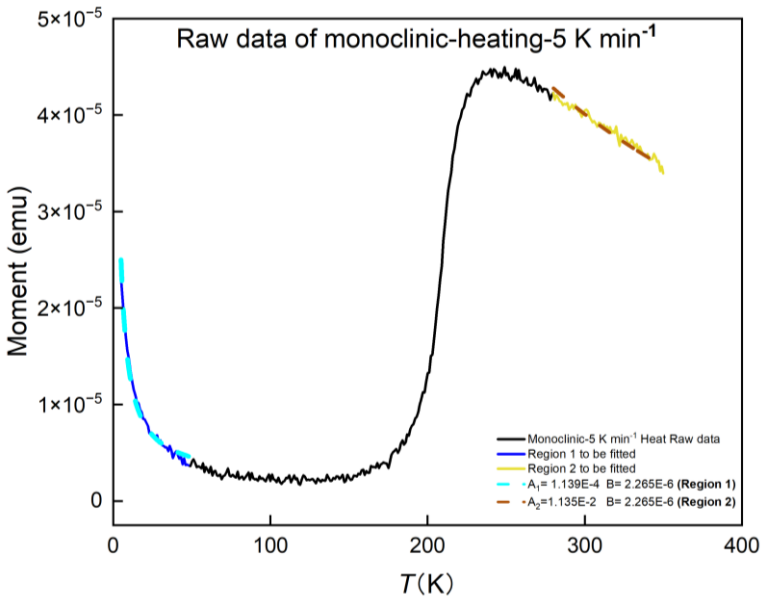

Figure 32. The raw data of the magnetic moment (emu) vs. *T* during the heating process for the monoclinic polymorph of [^{57}Fe(PM-BiA)$_2$(NCS)$_2$] was recorded at a scanning rate of 5 K min^{-1}.

4.3.2 Magnetic Properties of Two Phases of [^{57}Fe(PM-BiA)$_2$(NCS)$_2$]

The magnetic properties of two phases of [^{57}Fe(PM-BiA)$_2$(NCS)$_2$] was illustrated using plots of molar magnetic susceptibility $\boldsymbol{\chi T}$ versus temperature $\boldsymbol{T}$. The calculation for molar magnetic susceptibility $\boldsymbol{\chi T}$ with correction (*Section 4.3.1)* is as following:

$$\boldsymbol{\chi T}\left(\mathbf{cm^3\ K\ mol^{-1}}\right) = \frac{\boldsymbol{\chi}_{corr.}\left(\mathbf{emu} = \frac{\mathbf{cm^3}}{\mathbf{Oe}}\right) * \boldsymbol{T}(\mathbf{K}) * \mathbf{Molecular\ Weight\ (g)}}{\mathbf{Magnetic\ field\ (Oe)} * \mathbf{Sample\ Mass\ (g)}} \qquad (11)$$

As mentioned in *Section 1.1*, the orthorhombic polymorph exhibits an abrupt spin transition, in temperature range from 170 to 178 K while the monoclinic polymorph shows a gradual spin transition in temperature range from150 to 250 K. As shown in *Figure 33*, the results for the two phases of [^{57}Fe(PM-BiA)$_2$(NCS)$_2$] match these expectations. According to the literature, the $\boldsymbol{\chi T}$ for HS-state Fe^{2+} ions is approximately 3.5 cm^{-3} K mol^{-1} at room temperature, decreasing to around 0 at 80 K.[16]

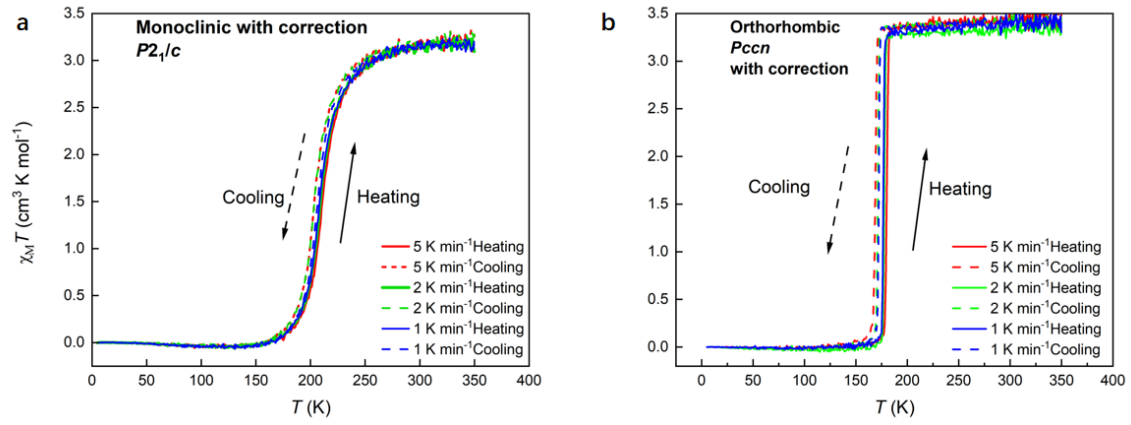

Figure 33. $\boldsymbol{\chi T}$ versus temperature $\boldsymbol{T}$ plots of monoclinic of [^{57}Fe(PM-BiA)$_2$(NCS)$_2$] (a) orthorhombic of [^{57}Fe(PM-BiA)$_2$(NCS)$_2$] (b). The cooling and heating procedures are shown in dashed lines and solid lines, respectively. The scan rates are 5 K min^{-1}(red), 2 K min^{-1}(green), and 1 K min^{-1} (blue).

Figure 33 shows that the SCO materials [^{57}Fe(PM-BiA)$_2$(NCS)$_2$] exhibit hysteresis. The hysteresis loop width ΔT, is defined as the difference between $T_{1/2}\uparrow$ during the heating process and $T_{1/2}\downarrow$during the cooling process. The HS fraction γ_{HS} represents the proportion of molecules in the HS state relative to the total and is calculated as follows:

$$\gamma_{HS} = \frac{\chi T - \chi T_{min}}{\chi T_{max} - \chi T_{min}} \quad (12)$$

The HS fraction γ_{HS} as a function of temperature is used to describe the behavior of the SCO material's spin-state change and hysteresis (*Figure 34*).

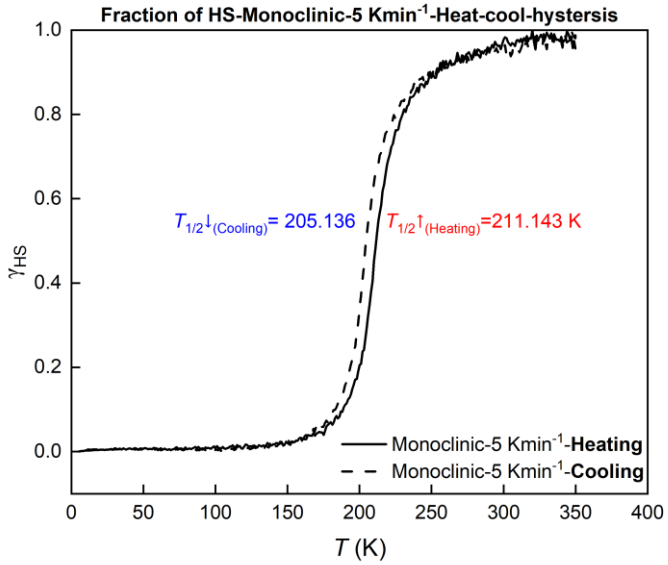

Figure 34. HS fraction γ_{HS} as a function of temperature (T) for the monoclinic polymorph of the[^{57}Fe(PM-BiA)$_2$(NCS)$_2$] during heating (solid line) and cooling process (dashed line), measured at a scan rate of 5 K min^{-1}. $T_{1/2}\uparrow$ is the temperature at which γ_{HS}=0.5 during heating process(red), $T_{1/2}\downarrow$ is the temperature at which γ_{HS}=0.5 during cooling process(blue).

Based on the example in *Figure 34*, the transition temperatures and hysteresis for the two polymorphs of [^{57}Fe(PM-BiA)$_2$(NCS)$_2$] at scan rates of 5, 2, and 1 K min^{-1} are summarized in *Table 5*. These values are compared with the reference data for corresponding [Fe(PM-BiA)$_2$(NCS)$_2$] samples at the same scan rates.[6] The hysteresis of the two polymorphs of [^{57}Fe(PM-BiA)$_2$(NCS)$_2$] with scan rate of 2 and 1 K min^{-1} is nearly identical with the reference values for the corresponding polymorphs of [Fe(PM-BiA)$_2$(NCS)$_2$].[6] Only a small deviation around 1 K can be found while cooling with a scan rate of 5 K min^{-1}. It may be induced by the non-equilibrium thermal condition when the scan rate is too fast.

Table 6. Comparison of $T_{1/2}\uparrow$, $T_{1/2}\downarrow$ and hysteresis ΔT for the monoclinic and orthorhombic polymorphs of [^{57}Fe(PM-BiA)$_2$(NCS)$_2$] and reference data [6] of [Fe(PM-BiA)$_2$(NCS)$_2$] at different scan rates.

Sample	Polymorphs	Scan rate (K min^{-1})	$T_{1/2}\uparrow$ (K)	$T_{1/2}\downarrow$ (K)	Hysteresis ΔT
[^{57}Fe(PM-BiA)$_2$(NCS)$_2$]	Monoclinic	5	211.143	205.136	6.007
		2	209.302	205.911	3.391
		1	208.430	206.783	1.647
	Orthorhombic	5	180.620	169.283	11.337
		2	178.199	171.221	6.988
		1	177.035	171.802	5.233
[Fe(PM-BiA)$_2$(NCS)$_2$][6]	Monoclinic	5	211.110	203.660	7.450
		2	209.310	205.760	3.550
		1	208.611	206.520	2.091
	Orthorhombic	5	180.91	168.37	12.540
		2	178.53	171.07	7.460
		1	177.51	172.18	5.330

Additionally, the data above in *Table 6* and are plotted to present the linear relationship between transition temperature and scan rate, allowing for a comparison between the two polymorphs of [^{57}Fe(PM-BiA)$_2$(NCS)$_2$] and [Fe(PM-BiA)$_2$(NCS)$_2$] in Figure *35*. For the monoclinic polymorph, the hysteresis for [^{57}Fe(PM-BiA)$_2$(NCS)$_2$] increases from 1.647 K to 6.007 K (ΔT = 4.360 K) with increasing scan rate, while it increases from 2.091 K to 7.450 K (ΔT = 5.359 K) for [Fe(PM-BiA)$_2$(NCS)$_2$], as shown in *Figure 35a.* Meanwhile, the orthorhombic polymorph [^{57}Fe(PM-BiA)$_2$(NCS)$_2$] shows an increase from 5.223 K to 11.337 K (ΔT = 6.114 K), whereas [Fe(PM-BiA)$_2$(NCS)$_2$] increases from 5.330 K to 12.540 K (ΔT = 7.21 K) (*Figure 35b*).

It is evident that the hysteresis width increases with the scan rate, consistent with the behavior reported in the literature for [Fe(PM-BiA)$_2$(NCS)$_2$]. [6] At a scan rate of 5 K min^{-1}, the hysteresis width for [^{57}Fe(PM-BiA)$_2$(NCS)$_2$] is slightly larger compared to that of [Fe(PM-BiA)$_2$(NCS)$_2$].

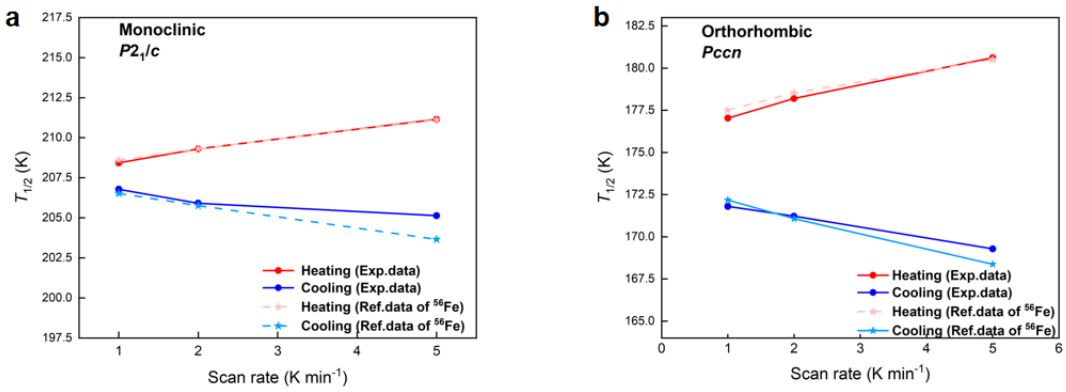

Figure 35. Transition temperature $T_{1/2}$ over scan rate for the monoclinic (a) and orthorhombic (b) polymorphs [^{57}Fe(PM-BiA)$_2$(NCS)$_2$] and [Fe(PM-BiA)$_2$(NCS)$_2$].The experimental data of [^{57}Fe(PM-BiA)$_2$(NCS)$_2$] are shown as solid lines with dots. The reference data [6] of [Fe(PM-BiA)$_2$(NCS)$_2$] are shown by dashed lines, with stars (red, pink-heating and blue, pale blue-cooling).

4.4 The Results and Mechanism of Catalytic Oxidation of 2-Picoline

Compared to the reference, the experimental FT-IR results (*Section 3.6*) show that the product $[NH_4]_3[CrMo_6O_{18}(OH)_6]\cdot 7H_2O$ contains characteristic shifts in the NH, Mo=O, and Mo-O-Mo bands, indicating slight changes in the bonding environment. [59]

The experimental pattern shows several similar diffraction peaks at the same 2θ positions as the reference pattern, indicating that the synthesized sample is consistent with the reported phase and contains $[NH_4]_3[CrMo_6O_{18}(OH)_6]\cdot 7H_2O$.[58] However, the diffraction peaks in the experimental data appear broader and of lower intensity compared to the literature data, with an unstable background signal. This suggests that the sample may have smaller crystallite sizes and lower crystallinity, which could also be influenced by measurement conditions and equipment. Additionally, the experimental sample is $[NH_4]_3[CrMo_6O_{18}(OH)_6]\cdot 7H_2O$, while the literature sample is the anhydrous form $[NH_4]_3[CrMo_6O_{18}(OH)_6]$. This difference may account for the presence of water molecules in the hydrate. They may cause slight changes in lattice parameters, thereby affecting the position and width of the diffraction peaks. Furthermore, the water molecules in the hydrate could contribute to additional background noise.

The reaction mechanism from the literature, was identified through the structural analysis of intermediates and reaction products by ^{1}H NMR spectroscopy. The possible mechanism (*Figure 36*) for the catalytic oxidation of 2-picoline is as follows:[59]

- Catalyst Activation: Catalyst **1**, a polyoxometalate (POM) complex containing chromium and molybdenum, reacts with 2.0 equivalents of hydrogen peroxide to form the peroxo anion **D**.

- Catalytic Oxidation of 2-picoline to alcohol: The substrate, 2-picoline, reacts with the activated catalyst. A proton from the methyl group of the substrate inserts into one of the peroxo groups of **D**, forming intermediate **E**. Intermediate E releases 2-pyridinemethanol and produces intermediate **F**.
- Oxidation of 2-pyridinemethanol to aldehyde: 2-Pyridinemethanol further reacts with intermediate F. A proton from the alcohol group inserts into one of the peroxo groups of **F**. The peroxo group of F interacts with the -CH_2 group of 2-pyridinemethanol, forming intermediate **G**. One α-hydrogen at the benzylic position combines with an $^{-}$OH ion of the peroxo group, producing H_2O. The Mo−O−CH bond breaks, yielding the aldehyde. Catalyst **1** re-enters the catalytic cycle.[59]

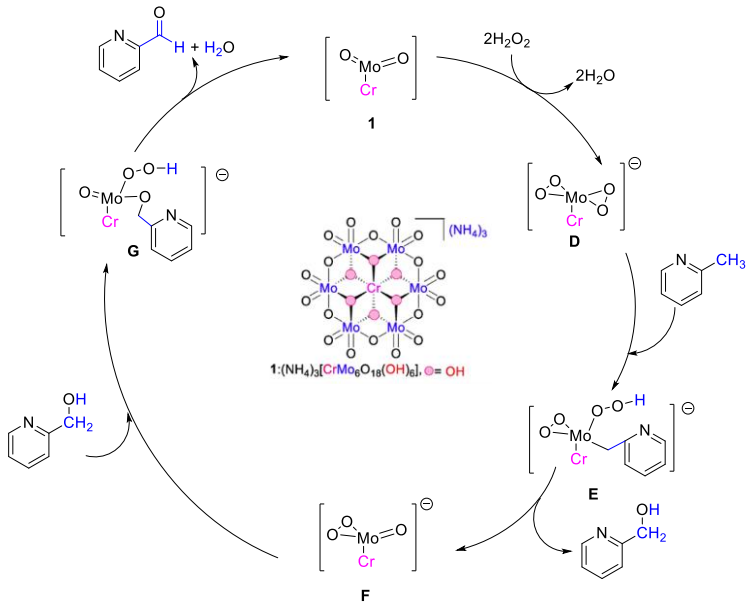

Figure 36. Possible reaction mechanism for the catalytic oxidation of 2-picoline to an aldehyde.

The TLC analysis under UV light shows three distinct spots (*Figure 37*). The first spot on the left corresponds to 2-picoline, the second spot in the middle represents the reaction mixture, and the third spot on the right is the target product (pyridine-2-carbaldehyde). The positions and intensities of the spots indicate that the target product is absent in the reaction mixture, suggesting that the reaction has not progressed to form aldehyde.

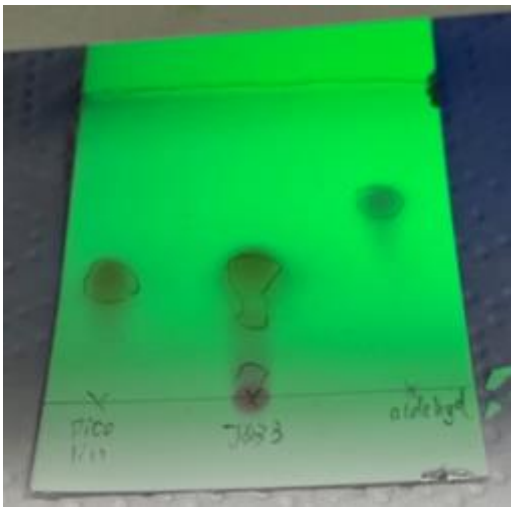

Figure 37. The TLC analysis of the catalytic oxidation of 2-picoline.

During the reaction, the color changes observed may correspond to different stages in the catalytic cycle, possibly related to changes in the oxidation states of the metal centers (chromium or molybdenum) or the formation of intermediates. However, these color changes do not necessarily indicate the formation of the target product. They may simply suggest the formation of intermediates or changes in catalyst activity, rather than completion of the reaction or production of the desired compound. TLC analysis was conducted under various reaction conditions, as shown in the *Table 7*, indicating that the conditions or reaction time were insufficient to achieve the synthesis of the target product.

Table 7. Screening of solvent, catalyst loading and temperature of the catalytic oxidation of 2-Pyridinecarboxaldehyde from 2-Picoline with catalyst 1.

Entry	Solvent	Oxidant	Temperature (°C)	Cat. loading Mol %	Reaction Time (min)	Yield %
1	H_2O	30% H_2O_2	55	1.0	15	0
2	H_2O	30% H_2O_2	55	1.0	30	0
3	H_2O	30% H_2O_2	55	1.0	60	0
4	H_2O	30% H_2O_2	55	1.0	120	0

5. Conclusions

In this study, Powder X-ray Diffraction (PXRD) and Physical Property Measurement System (PPMS) measurements were utilized to investigate the isotope effect on the structural and physical properties of the orthorhombic and monoclinic polymorphs of the previously reported Spin-crossover (SCO) compound [Fe(PM-Bia)$_2$(NCS)$_2$]. Specifically, the study involved the substitution of ^{nat}Fe with ^{57}Fe and partial deuteration of the compound, while also exploring catalytic oxidation methods to convert 2-picoline to pyridine-2-carbaldehyde. The synthesis of the two polymorphs of [Fe(PM-Bia)$_2$(NCS)$_2$] was optimized using ^{nat}Fe, with reaction conditions adjusted to achieve the highest yield and control over the phase. The PXRD analysis was performed to confirm the successful synthesis of the two polymorphs of [Fe(PM-Bia)$_2$(NCS)$_2$]. The results turns out that the monoclinic phase is nearly pure, while the orthorhombic phase contains a small amount of impurities.

Subsequently, a small amount of impurities was observed during the synthesis of the orthorhombic phase of [^{57}Fe(PM-Bia)$_2$(NCS)$_2$]. Structural comparisons using two different PXRD systems, along with the analysis of PXRD patterns and comparisons with the literature values for [Fe(PM-BiA) $_2$(NCS)$_2$], demonstrate that the isotope effect had a slight impact on the structure, resulting in only slight changes in the lattice parameters and unit cell volume.

PPMS measurements were performed on both polymorphs of [^{57}Fe(PM-Bia)$_2$(NCS)$_2$] to study their spin transitions. The orthorhombic polymorph exhibited an abrupt transition, while the monoclinic polymorph showed a gradual transition. During both cooling and heating cycles, more than 90% of the molecules underwent a spin state transition between the low-spin (LS) and high-spin (HS) states within approximately 1.5 K. The thermal hysteresis widths of both polymorphs were measured, showing minor variations, with the transitions completing around 8 K and 100 K, respectively.

Regarding the catalytic oxidation, while a catalyst was successfully synthesized, it did not effectively control the oxidation of 2-picoline to the aldehyde stage. In future research, we will explore alternative methods to achieve complete deuteration of the ligand, aiming for full deuteration of the entire compound. In the case of a fully deuterated SCO compound [Fe(PM-Bia)2(NCS)2], a stronger isotope effect can be expected due to the mass ratio of hydrogen isotopes being 2:1, compared to the mass ratio of 57:56 (approximately 1.02) for iron. This will enable us to perform further tests to observe any structural or physical property changes induced by the isotope effect.

Furthermore, the findings of this study open avenues for exploring the use of isotope effects in fine-tuning the structural and physical properties of SCO compounds. The slight modifications in cell parameters and spin state transitions observed here suggest that isotope effect could potentially be used to regulate SCO systems.

6. Appendix

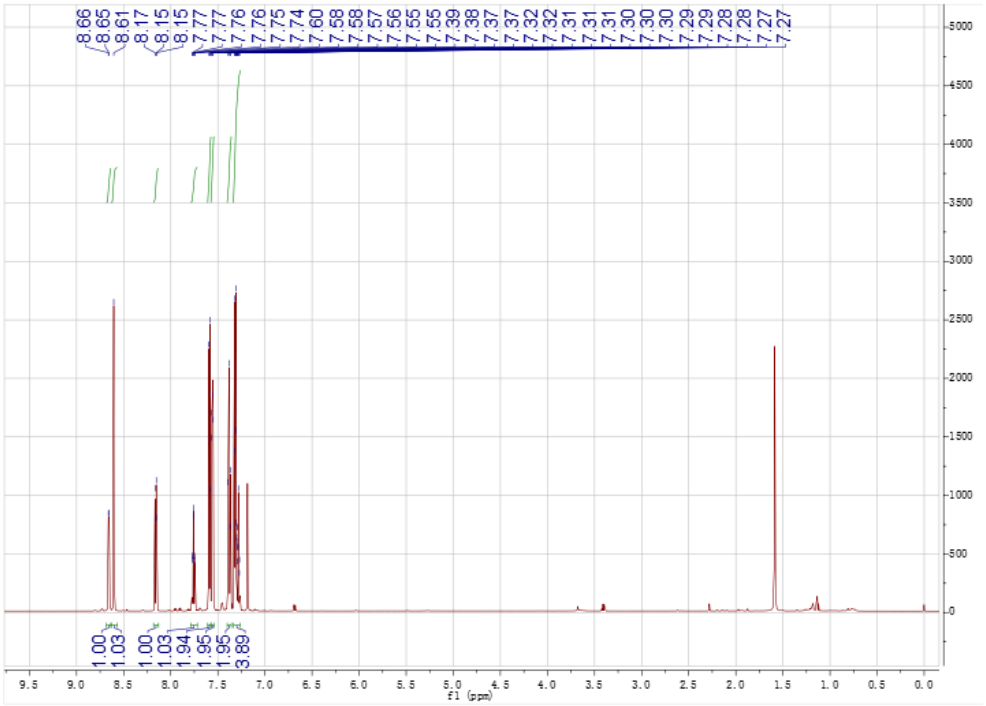

Figure 38. The ^{1}H NMR spectrum (600MHz, $CDCl_3$) of N-(2'-pyridylmethylene)-4-aminobiphenyl.

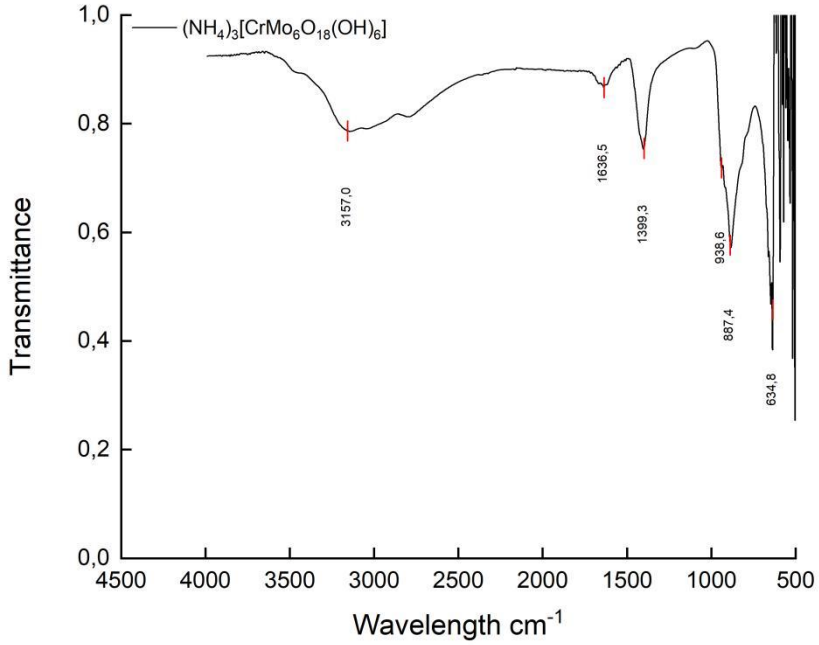

Figure 39. FT-IR spectra of $[NH_4]_3[CrMo_6O_{18}(OH)_6]\bullet 7H_2O$.

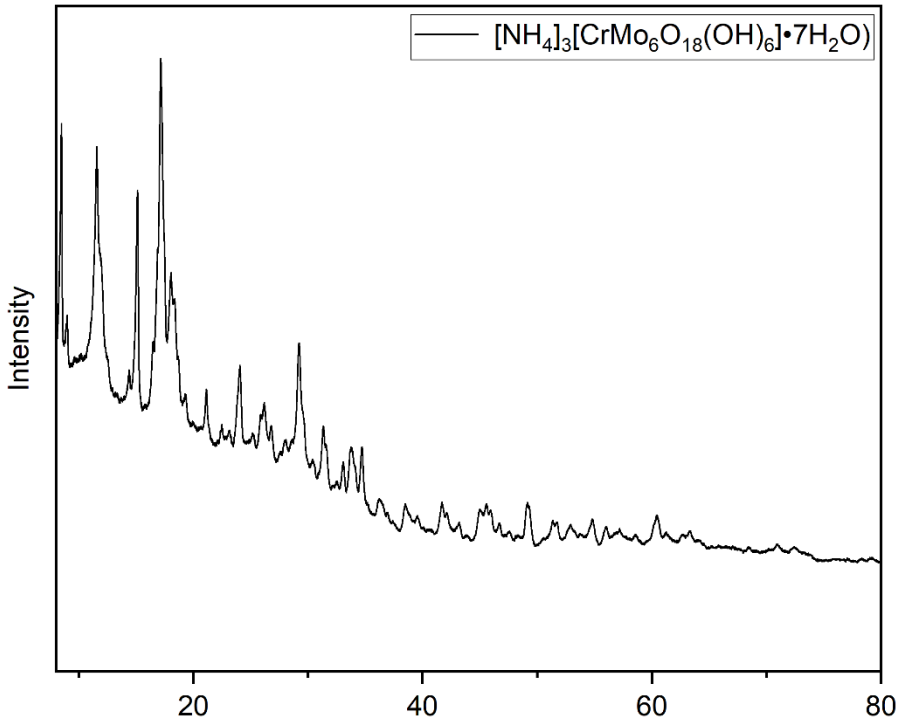

Figure 40. PXRD plot of $[NH_4]_3[CrMo_6O_{18}(OH)_6]\cdot 7H_2O$ using the xHuber device.

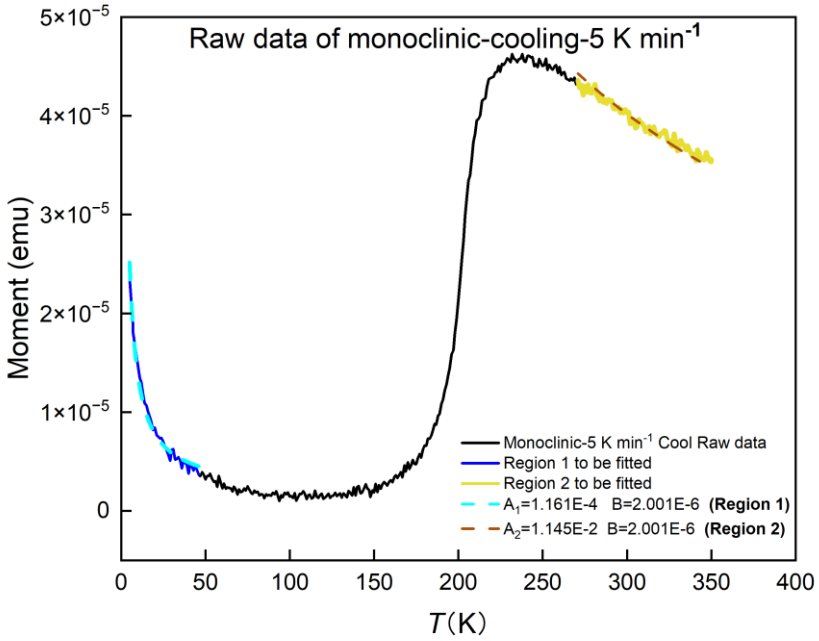

Figure 41. The raw data of the magnetic moment (emu) vs. *T* during the cooling process for the monoclinic polymorph of $[^{57}Fe(PM\text{-}BiA)_2(NCS)_2]$ was recorded at a scanning rate of 5 K min^{-1}.

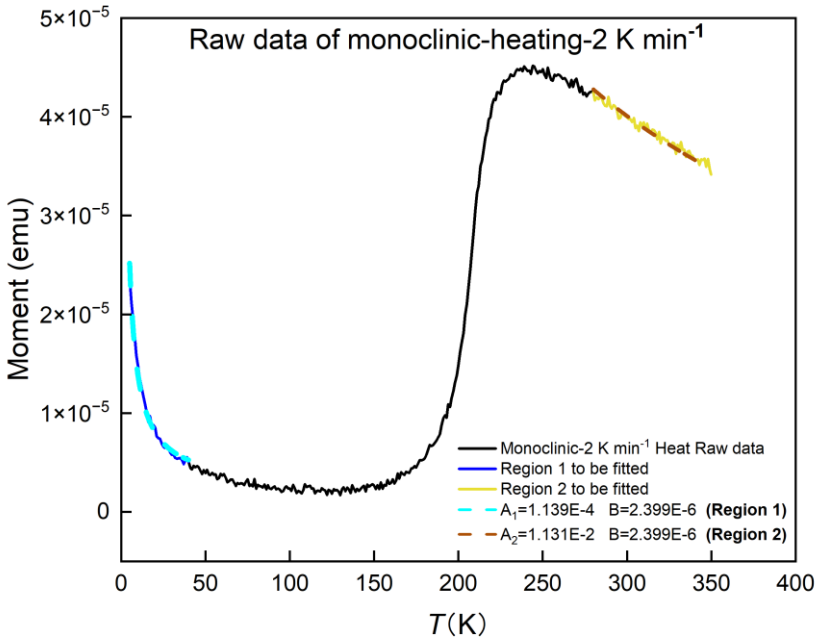

Figure 42. The raw data of the magnetic moment (emu) versus temperature during the heating process for the monoclinic polymorph of [^{57}Fe(PM-BiA)$_2$(NCS)$_2$] was recorded at a scanning rate of 2 K min^{-1}.

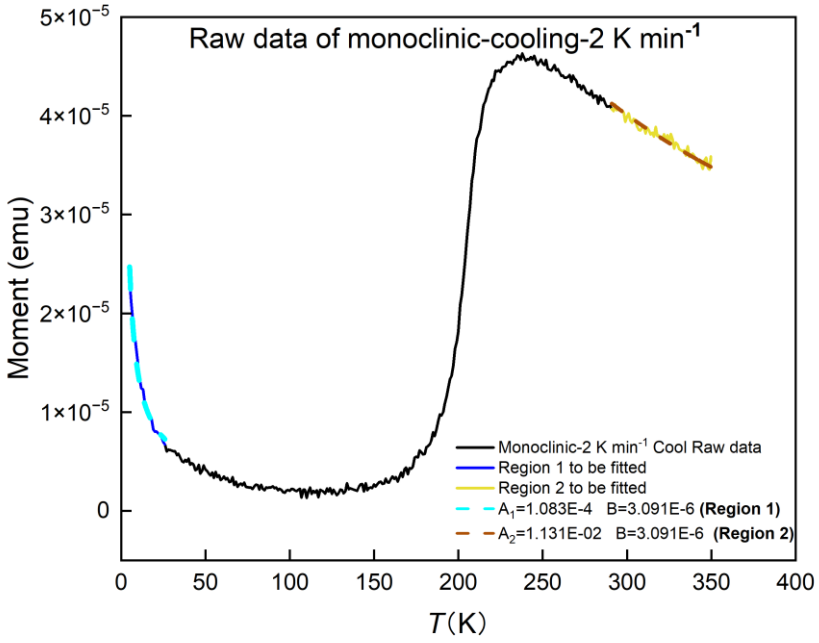

Figure 43. The raw data of the magnetic moment (emu) versus temperature during the cooling process for the monoclinic polymorph of [^{57}Fe(PM-BiA)$_2$(NCS)$_2$] was recorded at a scanning rate of 2 K min^{-1}.

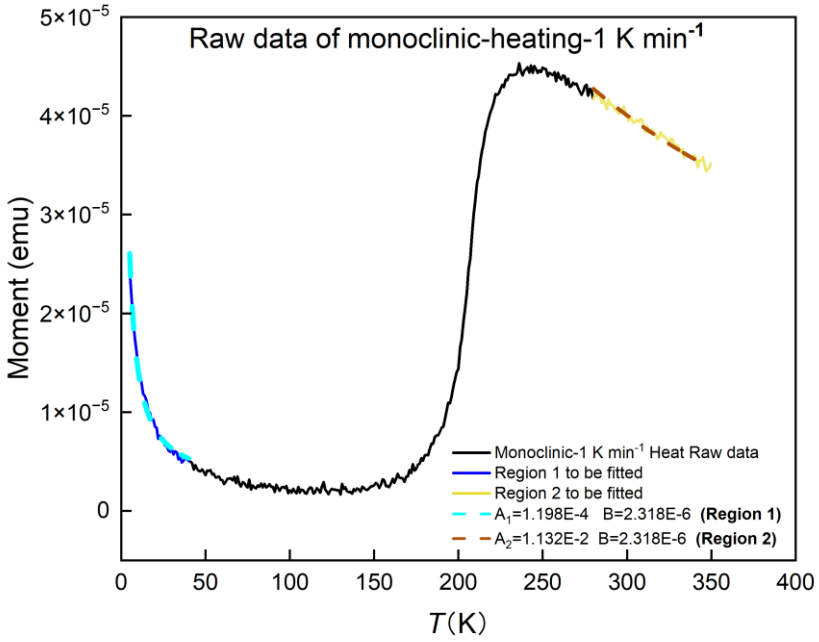

Figure 44. The raw data of the magnetic moment (emu) versus temperature during the heating process for the monoclinic polymorph of [^{57}Fe(PM-BiA)$_2$(NCS)$_2$] was recorded at a scanning rate of 1 K min^{-1}.

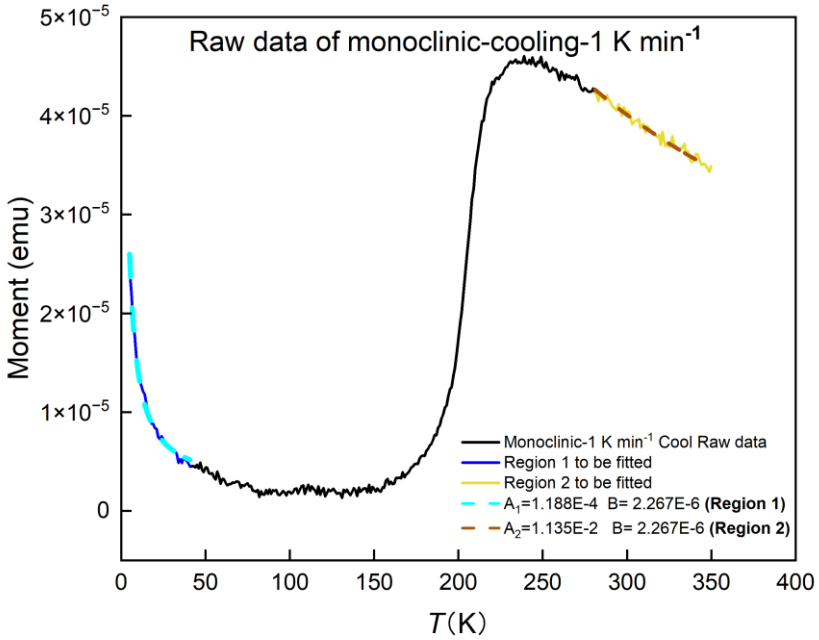

Figure 45. The raw data of the magnetic moment (emu) versus temperature during the cooling process for the monoclinic polymorph of [^{57}Fe(PM-BiA)$_2$(NCS)$_2$] was recorded at a scanning rate of 1 K min^{-1}.

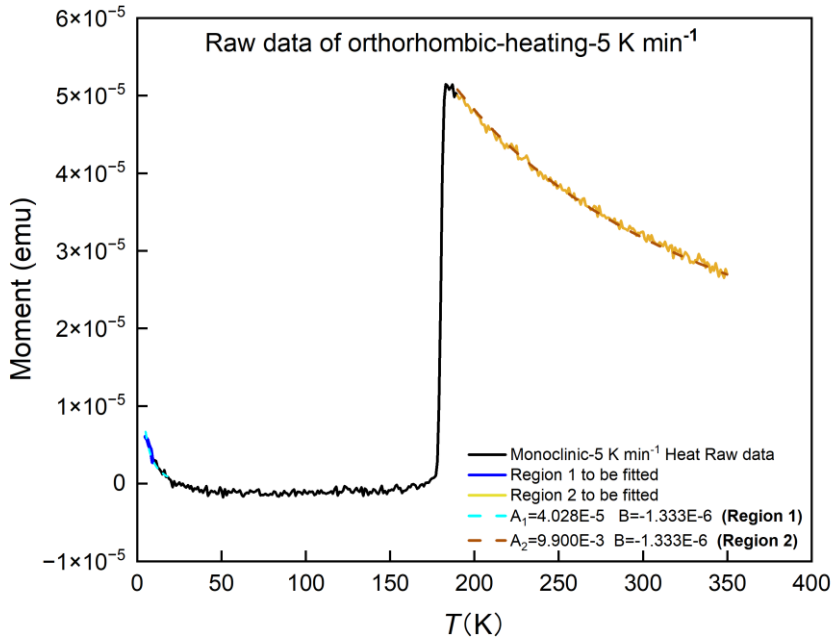

Figure 46. The raw data of the magnetic moment (emu) versus temperature during the heating process for the orthorhombic polymorph of [^{57}Fe(PM-BiA)$_2$(NCS)$_2$] was recorded at a scanning rate of 5 K min^{-1}.

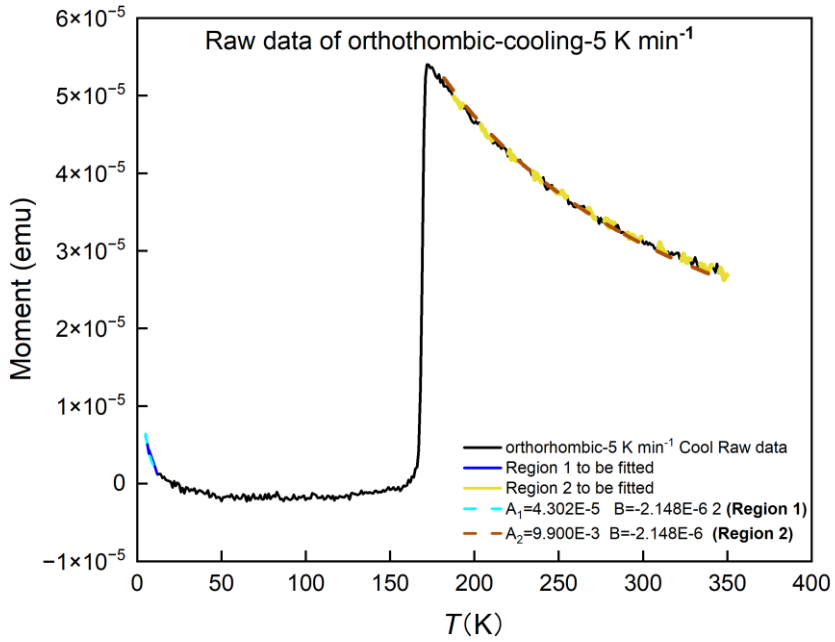

Figure 47. The raw data of the magnetic moment (emu) versus temperature during the cooling process for the orthorhombic polymorph of [^{57}Fe(PM-BiA)$_2$(NCS)$_2$] was recorded at a scanning rate of 5 K min^{-1}.

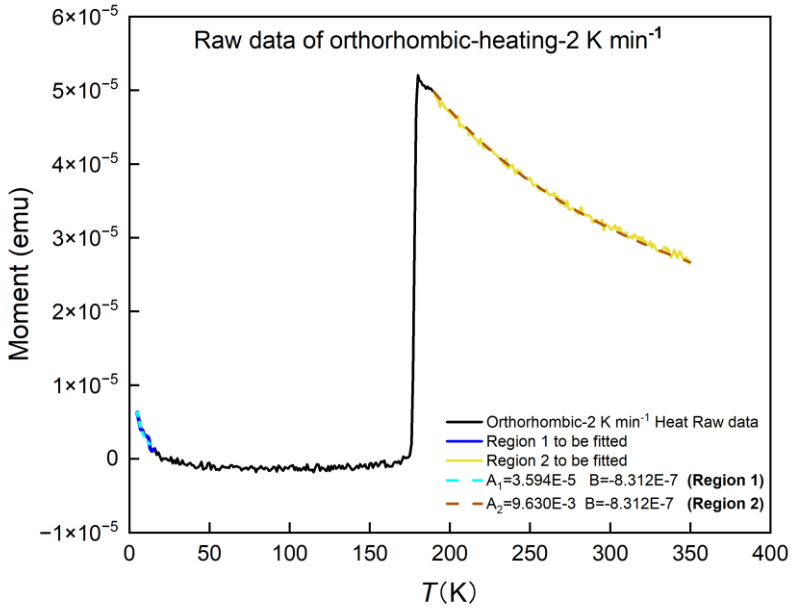

Figure 48. The raw data of the magnetic moment (emu) versus temperature during the heating process for the orthorhombic polymorph of [^{57}Fe(PM-BiA)$_2$(NCS)$_2$] was recorded at a scanning rate of 2 K min^{-1}.

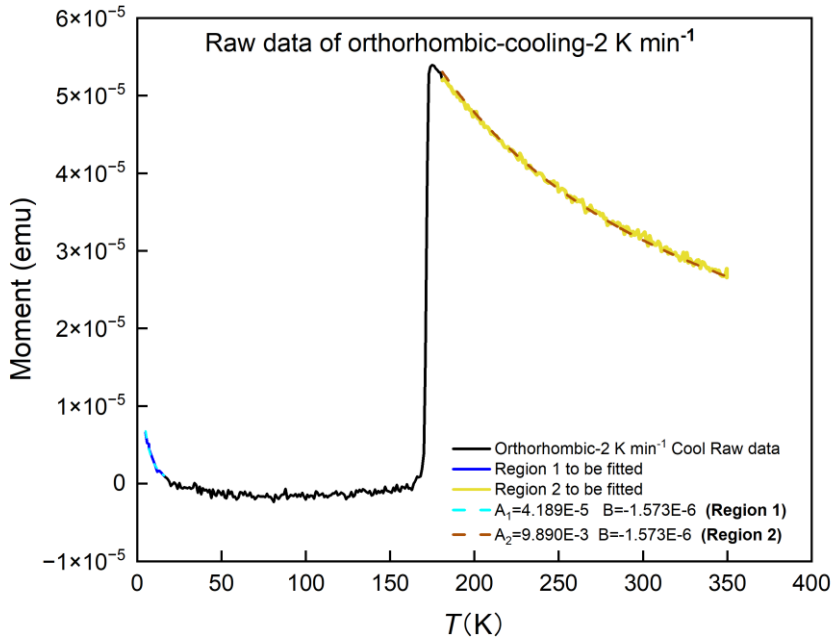

Figure 49. The raw data of the magnetic moment (emu) versus temperature during the cooling process for the orthorhombic polymorph of [^{57}Fe(PM-BiA)$_2$(NCS)$_2$] was recorded at a scanning rate of 2 K min^{-1}.

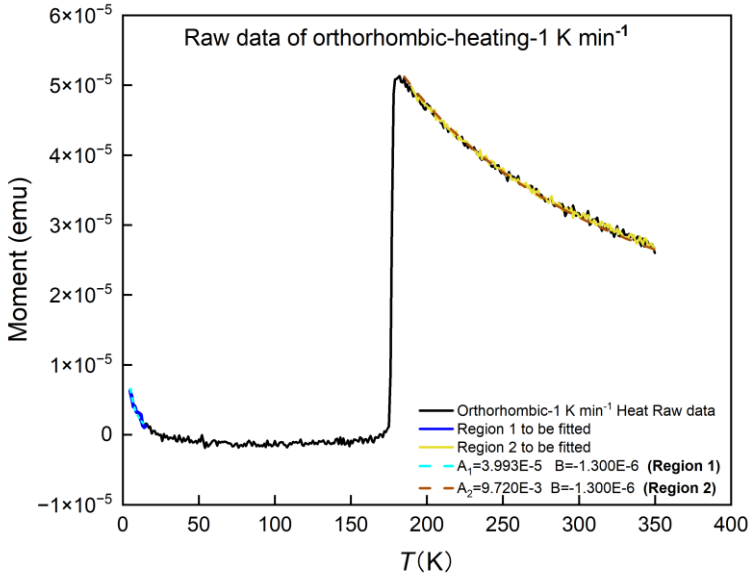

Figure 50. The raw data of the magnetic moment (emu) versus temperature during the heating process for the orthorhombic polymorph of [^{57}Fe(PM-BiA)$_2$(NCS)$_2$] was recorded at a scanning rate of 1 K min^{-1}.

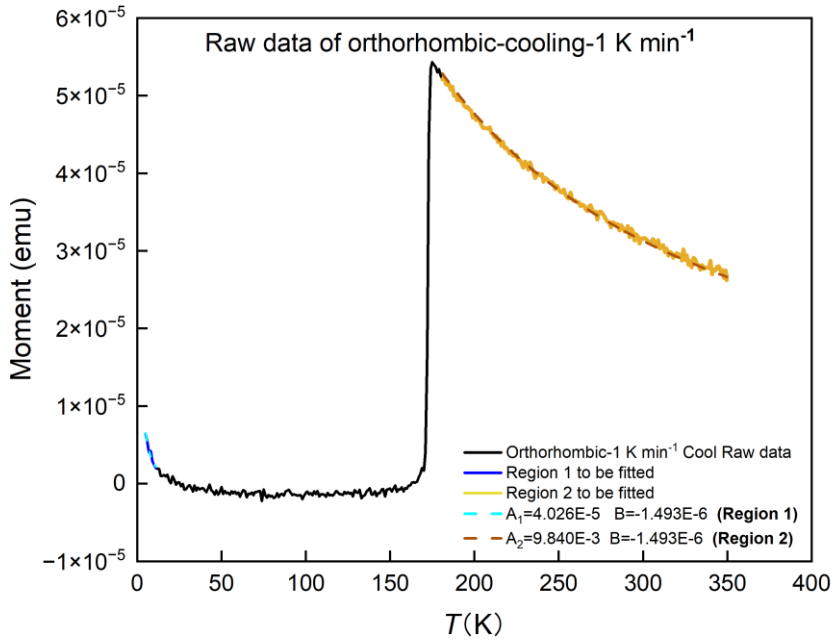

Figure 51. The raw data of the magnetic moment (emu) versus temperature during the cooling process for the orthorhombic polymorph of [^{57}Fe(PM-BiA)$_2$(NCS)$_2$] was recorded at a scanning rate of 1 K/min^{-1}.

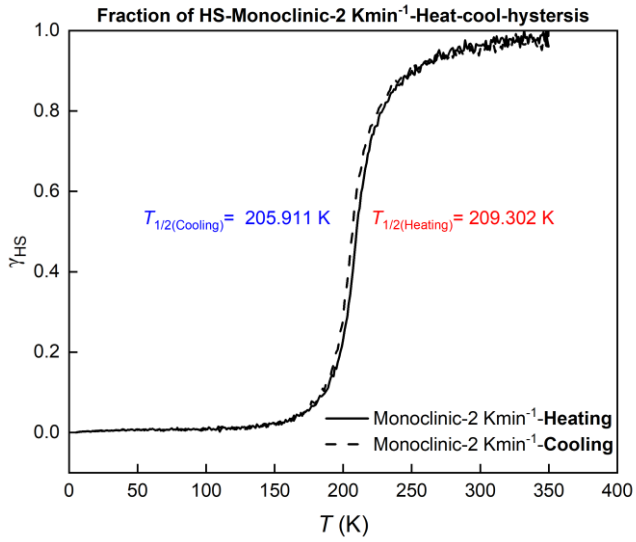

Figure 52. HS fraction γ_{HS} as a function of temperature (T) for the monoclinic polymorph of the[^{57}Fe(PM-BiA)$_2$(NCS)$_2$] during heating (solid line) and cooling process (dashed line), measured at a scan rate of 2 K min^{-1}. $T_{1/2}\uparrow$ is the temperature at which γ_{HS}=0.5 during heating process(red), $T_{1/2}\downarrow$ is the temperature at which γ_{HS}=0.5 during cooling process(blue).

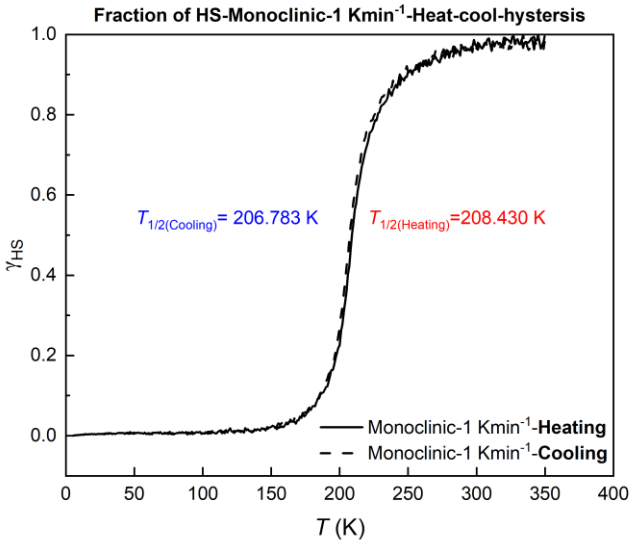

Figure 53. HS fraction γ_{HS} as a function of temperature (T) for the monoclinic polymorph of the[^{57}Fe(PM-BiA)$_2$(NCS)$_2$] during heating (solid line) and cooling process (dashed line), measured at a scan rate of 1 K min^{-1}. $T_{1/2}\uparrow$ is the temperature at which γ_{HS}=0.5 during heating process(red), $T_{1/2}\downarrow$ is the temperature at which γ_{HS}=0.5 during cooling process (blue).

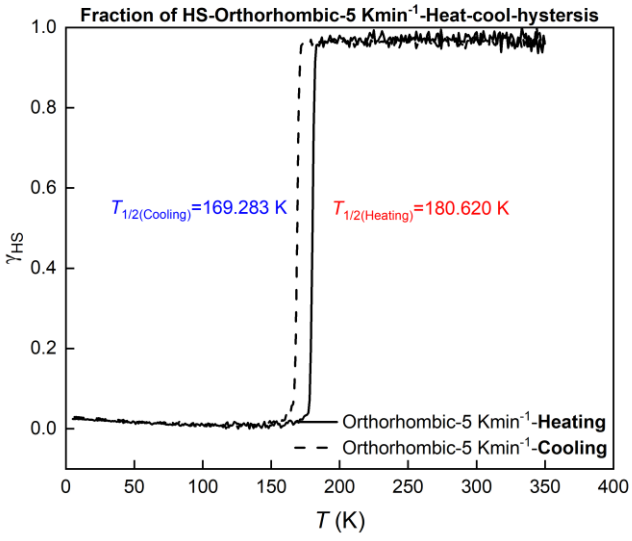

Figure 54. HS fraction γ_{HS} as a function of temperature (T) for the orthorhombic polymorph of the[^{57}Fe(PM-BiA)$_2$(NCS)$_2$] during heating (solid line) and cooling process (dashed line), measured at a scan rate of 5 K min^{-1}. $T_{1/2}\uparrow$ is the temperature at which γ_{HS}=0.5 during heating process(red), $T_{1/2}\downarrow$ is the temperature at which γ_{HS}=0.5 during cooling process(blue).

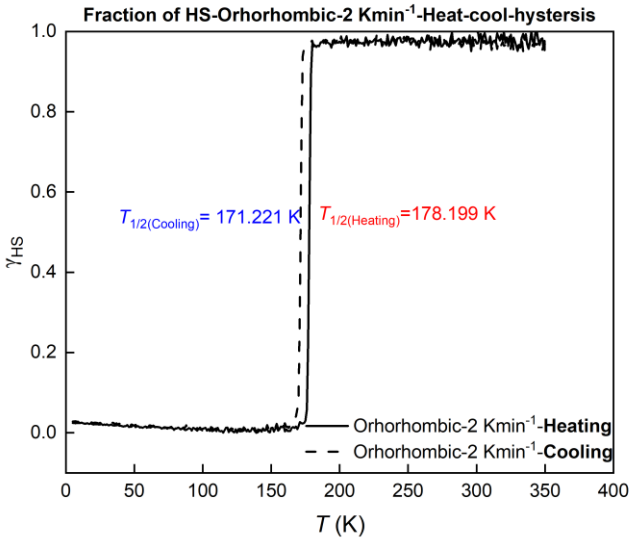

Figure 55. HS fraction γ_{HS} as a function of temperature (T) for the orthorhombic polymorph of the[^{57}Fe(PM-BiA)$_2$(NCS)$_2$] during heating (solid line) and cooling process (dashed line), measured at a scan rate of 2 K min^{-1}. $T_{1/2}\uparrow$ is the temperature at which γ_{HS}=0.5 during heating process(red), $T_{1/2}\downarrow$ is the temperature at which γ_{HS}=0.5 during cooling process(blue).

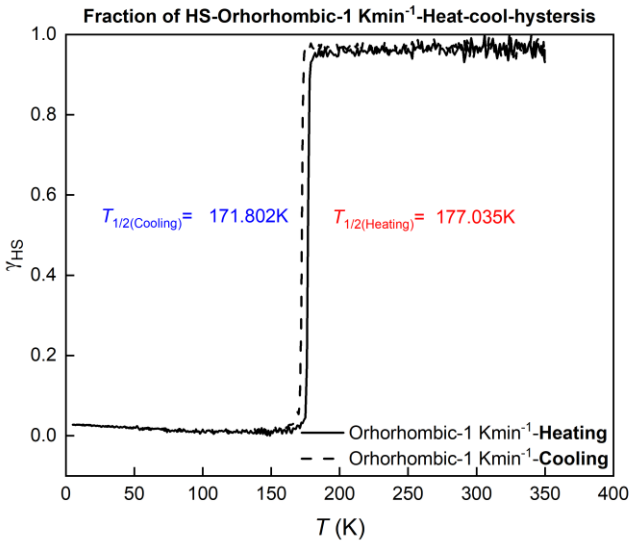

Figure 56. HS fraction γ_{HS} as a function of temperature (T) for the orthorhombic polymorph of the[^{57}Fe(PM-BiA)$_2$(NCS)$_2$] during heating (solid line) and cooling process (dashed line), measured at a scan rate of 1 K min^{-1}. $T_{1/2}\uparrow$ is the temperature at which γ_{HS}=0.5 during heating process(red), $T_{1/2}\downarrow$ is the temperature at which γ_{HS}=0.5 during cooling process(blue).

6.1 List of Abbreviations and Symbols

PPMS	Physical property measurement system
NMR	Nuclear magnetic resonance
TLC	Thin layer chromatography
PXRD	X-ray powder diffraction
LFT	Ligand field theory
FT-IR	Fourier transform infrared spectroscopy
PM-BiA	N-2'-pyridylmethylene-4-(aminobiphenyl)
NCS	Thiocyanato
SCO	Spin crossover
LS	Low-spin
HS	High-spin
$P2_1/c$	Monoclinic
Pccn	Orthorhombic
γ_{HS}	Fraction of molecules in the high-spin state
P	Spin pairing energy
Δ_o	Crystal field splitting energy
2-pic	2-picolylamine
Sol	C_2H_5OD and CH_3OD
L	2,6-di(pyrazol-1-yl)pyridine
pz	pyrazolyl
phen	1,10-phenanthroline
λ	Wavelength of the X-rays
d	Distance between atomic planes in the crystal lattice
θ	Angle between the incident wave and the scattering plane
n	Order of diffraction
$F(hkl)$	Atomic scattering factor of the *j*-th atom,
f_j	Scattering factor of atom *j*
x_j,y_j,z_j	Coordinates of this atom within the unit cell
hkl	Miller indices of the crystallographic plane
r	Position vector from the nucleus to the electron cloud

ρ(r)	Electron density at position $\boldsymbol{r}$
q	Scattering vector
M	Magnetization strength
H	Magnetic field strength
T	Temperature
C	Curie constant
FM	ferromagnetism
AFM	antiferromagnetism
FIM	ferrimagnetism
$\boldsymbol{\varepsilon}$	induced electromotive force (voltage), with the unit of volts (V)
Φ_B	magnetic flux passing through the coil, with the unit of webers (Wb)
$\frac{d_{\phi_B}}{d_t}$	rate of change of magnetic flux over time
VSM	Vibrating Sample Magnetometer
FCC	Field-Cooled Cooling
FCWM	Field-Cooled Warming
EA	Ethyl acetate
R_p	Fitting error
R_{wp}	Weighted profile fitting error
I_{obs}	Observed intensities
I_{cal}	Calculated intensities
$\chi_{meas.}$	Total measured magnetic susceptibility
$\chi_{para.}$	Paramagnetic magnetic susceptibility
$\chi_{dia.}$	Diamagnetic magnetic susceptibility
A	Paramagnetic contribution
B	Diamagnetic contributions from the plastic sample holder
χT	Molar magnetic susceptibility
$T_{1/2}\uparrow$	The transition temperature where half of the molecules are in the high-spin state during the heating process
$T_{1/2}\downarrow$	The transition temperature where half of the molecules are in the high-spin state during the cooling process
ΔT	Temperature difference between $T_{1/2}\uparrow$ and $T_{1/2}\downarrow$

K	Kelvin
Oe	Oersted
°C	Grad celsius
min	Minute
MHz	Megahertz

6.2 List of Tables / Equations / Figures

Tables:

Equations:

Figure 32. The raw data of the magnetic moment (emu) vs. *T* during the heating process for the monoclinic polymorph of [^{57}Fe(PM-BiA)$_2$(NCS)$_2$] was recorded at a scanning rate of 5 K min^{-1}.

Figure 33. χT versus temperature T plots of monoclinic of [^{57}Fe(PM-BiA)$_2$(NCS)$_2$] (a) orthorhombic of [^{57}Fe(PM-BiA)$_2$(NCS)$_2$] (b).The scan rates are 5 K min^{-1}(red), 2 K min^{-1}(green), and 1K min^{-1}((blue).

Figure 34. HS fraction γ_{HS} as a function of temperature (*T*) for the monoclinic polymorph of the[^{57}Fe(PM-BiA)$_2$(NCS)$_2$] during heating (solid line) and cooling process (dashed line), measured at a scan rate of 5 K min^{-1}. $T_{1/2}\uparrow$ is the temperature at which γ_{HS}=0.5 during heating process(red), $T_{1/2}\downarrow$ is the temperature at which γ_{HS}=0.5 during cooling process(blue).

Figure 35. Transition temperature $T_{1/2}$ over scan rate for the monoclinic (a) and orthorhombic (b) polymorphs [^{57}Fe(PM-BiA)$_2$(NCS)$_2$] and [Fe(PM-BiA)$_2$(NCS)$_2$].The experimental data of [^{57}Fe(PM-BiA)$_2$(NCS)$_2$] are shown as solid lines with dots. The reference data of [Fe(PM-BiA)$_2$(NCS)$_2$] are shown by dashed lines, with stars (red, pink-heating and blue, pale blue-cooling).

Figure 36. Possible mechanism for the catalytic oxidation of 2-picoline to an aldehyde.

Figure 37. The TLC analysis of the catalytic oxidation of 2-picoline.

Figure 38. The ^{1}H-NMR spectrum (600MHz, $CDCl_3$) of N-(2'-Pyridylmethylene)-4-aminobiphenyl .

Figure 39. FT-IR spectra of $[NH_4]_3[CrMo_6O_{18}(OH)_6]\bullet 7H_2O$.

Figure 40. PXRD plot of $[NH_4]_3[CrMo_6O_{18}(OH)_6]\cdot 7H_2O$ using the xHuber device.

Figure 41. The raw data of the magnetic moment (emu) versus temperature during the cooling process for the monoclinic polymorph of [^{57}Fe(PM-BiA)$_2$(NCS)$_2$] was recorded at a scanning rate of 5 K min^{-1}.

Figure 42. The raw data of the magnetic moment (emu) versus temperature during the heating process for the monoclinic polymorph of [^{57}Fe(PM-BiA)$_2$(NCS)$_2$] was recorded at a scanning rate of 2 K min^{-1}.

Figure 43. The raw data of the magnetic moment (emu) versus temperature during the cooling process for the monoclinic polymorph of [^{57}Fe(PM-BiA)$_2$(NCS)$_2$] was recorded at a scanning rate of 2 K min^{-1}.

Figure 44. The raw data of the magnetic moment (emu) versus temperature during the heating process for the monoclinic polymorph of [^{57}Fe(PM-BiA)$_2$(NCS)$_2$] was recorded at a scanning rate of 1 K min^{-1}.

Figure 45. The raw data of the magnetic moment (emu) versus temperature during the cooling process for the monoclinic polymorph of [^{57}Fe(PM-BiA)$_2$(NCS)$_2$] was recorded at a scanning rate of 1 K min^{-1}.

Figure 46. The raw data of the magnetic moment (emu) versus temperature during the heating process for the orthorhombic polymorph of [^{57}Fe(PM-BiA)$_2$(NCS)$_2$] was recorded at a scanning rate of 5 K min^{-1}.

Figure 47. The raw data of the magnetic moment (emu) versus temperature during the cooling process for the orthorhombic polymorph of [^{57}Fe(PM-BiA)$_2$(NCS)$_2$] was recorded at a scanning rate of 5 K min^{-1}.

Figure 48. The raw data of the magnetic moment (emu) versus temperature during the heating process for the orthorhombic polymorph of [^{57}Fe(PM-BiA)$_2$(NCS)$_2$] was recorded at a scanning rate of 2 K min^{-1}.

Figure 49. The raw data of the magnetic moment (emu) versus temperature during the cooling process for the orthorhombic polymorph of [^{57}Fe(PM-BiA)$_2$(NCS)$_2$] was recorded at a scanning rate of 2 K/min^{-1}.

Figure 50. The raw data of the magnetic moment (emu) versus temperature during the heating process for the orthorhombic polymorph of [^{57}Fe(PM-BiA)$_2$(NCS)$_2$] was recorded at a scanning rate of 1 K min^{-1}.

Figure 51. The raw data of the magnetic moment (emu) versus temperature during the cooling process for the orthorhombic polymorph of [^{57}Fe(PM-BiA)$_2$(NCS)$_2$] was recorded at a scanning rate of 1 K min^{-1}.

Figure 52. HS fraction γ_{HS} as a function of temperature (T) for the monoclinic polymorph of the[^{57}Fe(PM-BiA)$_2$(NCS)$_2$] during heating (solid line) and cooling process (dashed line), measured at a scan rate of 2 K min^{-1}. $T_{1/2}\uparrow$ is the temperature at which γ_{HS}=0.5 during heating process(red), $T_{1/2}\downarrow$ is the temperature at which γ_{HS}=0.5 during cooling process(blue).

Figure 53. HS fraction γ_{HS} as a function of temperature (T) for the monoclinic polymorph of the[^{57}Fe(PM-BiA)$_2$(NCS)$_2$] during heating (solid line) and cooling process (dashed line), measured at a scan rate of 1 K min^{-1}. $T_{1/2}\uparrow$ is the temperature at which γ_{HS}=0.5 during heating process(red), $T_{1/2}\downarrow$ is the temperature at which γ_{HS}=0.5 during cooling process(blue).

Figure 54. HS fraction γ_{HS} as a function of temperature (T) for the orthorhombic polymorph of the[^{57}Fe(PM-BiA)$_2$(NCS)$_2$] during heating (solid line) and cooling process (dashed line), measured at a scan rate of 5 K min^{-1}. $T_{1/2}\uparrow$ is the temperature at which γ_{HS}=0.5 during heating process(red), $T_{1/2}\downarrow$ is the temperature at which γ_{HS}=0.5 during cooling process(blue).

Figure 55. HS fraction γ_{HS} as a function of temperature (T) for the orthorhombic polymorph of the[^{57}Fe(PM-BiA)$_2$(NCS)$_2$] during heating (solid line) and cooling process (dashed line), measured at a scan rate of 2 K min^{-1}. $T_{1/2}\uparrow$ is the temperature at which γ_{HS}=0.5 during heating process(red), $T_{1/2}\downarrow$ is the temperature at which γ_{HS}=0.5 during cooling process(blue).

Figure 56. HS fraction γ_{HS} as a function of temperature (T) for the orthorhombic polymorph of the[^{57}Fe(PM-BiA)$_2$(NCS)$_2$] during heating (solid line) and cooling process (dashed line),

measured at a scan rate of 1 K min^{-1}. $T_{1/2}\uparrow$ is the temperature at which γ_{HS}=0.5 during heating process(red), $T_{1/2}\downarrow$ is the temperature at which γ_{HS}=0.5 during cooling process(blue).

6.3 List of Chemicals and Reagents

Name	Supplier	Purity	CAS-No.
4-Aminobiphenyl	Thermo Scientific Chemicals	98 %	92-67-1
Pyridine-2-carboxalde-hyde	Thermo Scientific Chemicals	99%	1121-60-4
Acetic acid	VWR Chemicals	99-100%	64-19-7
Ethanol	VWR Chemicals	≥99,8% AnalaR NORMAPUR® ACS, Reag. Ph. Eur. analytical reagent	64-17-5
Diethyl ether	VWR Chemicals	≥99.7% AnalaR NORMAPUR® ACS, Reag. Ph. Eur. analytical reagent	60-29-7
Sulfuric acid solution 1M	Honeywell-Fluka	95.0 - 98.0 %	7664-93-9
Natriumbicarbonat	Sigma-Aldrich	*ReagentPlus*®, ≥99.5%	144-55-8
Celite® 545	Carl Roth	No details	68855-54-9
Kaliumthiocyanat	Sigma-Aldrich	Reagent Plus®, ⩾ 99.0%	333-20-0
L -Ascorbic acid	Sigma-Aldrich	99.0%	99 50-81-7

Methanol	VWR Chemicals	≥99.8% AnalaR NORMAPUR® ACS, Reag. Ph. Eur. analytisches Reagens	67-56-1
Ammoniummolybdat Tetrahydrat	Sigma-Aldrich	ACS reagent, 99.98% trace metals basis	12054-85-2
2-Methylpyridin	Sigma-Aldrich	98%	109-06-8
Hydrogen peroxide solution 30% (w/w)	Sigma-Aldrich	puriss. p.a., reag. ISO, reag. Ph. Eur.	7722-84-1
Ethylacetat	VWR Chemicals	⩾ 99,5%, AnalaR NORMAPUR® ACS, Reag. Ph. Eur. analytisches Reagens	141-78-6
Hexan (Isomerengemisch)	VWR Chemicals	HiPerSolv CHROMANORM® für die HPLC	110-54-3
Eisen(II)-sulfat Heptahydrat	Sigma-Aldrich	ACS reagent, ⩾ 99.0%	7782-63-0

7. References

[1] O. Kahn, C. J. Martinez, *Science* 1998, *279*, 44–48.

[2] L. Cambi, L. Szegö, *Berichte der deutschen chemischen Gesellschaft (A and B Series)* 1931, *64*, 2591–2598.

[3] W. A. Baker, H. M. Bobonich, *Inorganic Chemistry* 1964, *3*, 1184–1188.

[4] E. König, K. Madeja, *Chemical Communications (London)* 1966, *0*, 61–62.

[5] O. Kahn, J. Kröber, C. Jay, *Advanced Materials* 1992, *4*, 718–728.

[6] H. Shahed, N. Sharma, M. Angst, J. Voigt, J. Perßon, P. Prakash, K. W. Törnroos, D. Chernyshov, H. Gildenast, M. Ohl, et al., *Acta Crystallographica Section B Structural Science, Crystal Engineering and Materials* 2023, *79*, 354–367.

[7] P. Gütlich, A. B. Gaspar, Y. Garcia, V. Ksenofontov, *Comptes Rendus. Chimie* 2006, *10*, 21–36.

[8] K. Senthil Kumar, M. Ruben, *Coordination Chemistry Reviews* 2017, *346*, 176–205.

[9] P. Gütlich, A. B. Gaspar, Y. Garcia, *Beilstein Journal of Organic Chemistry* 2013, *9*, 342–391.

[10] H. Shahed, *Elucidation of Barocaloric Effect in Spin Crossover Compounds,* PhD thesis, RWTH, 2024.

[11] J. A. Real, A. B. Gaspar, V. Niel, M. C. Muñoz, *Coordination Chemistry Reviews* 2003, *236*, 121–141.

[12] J. A. Real, H. Bolvin, A. Bousseksou, A. Dworkin, O. Kahn, F. Varret, J. Zarembowitch, *Journal of the American Chemical Society* 1992, *114*, 4650–4658.

[13] A. Arroyave, A. Lennartson, A. Dragulescu-Andrasi, K. S. Pedersen, S. Piligkos, S. A. Stoian, S. M. Greer, C. Pak, O. Hietsoi, H. Phan, et al., *Inorganic Chemistry* 2016, *55*, 5904–5913.

[14] K. S. Murray, C. J. Kepert, *Topics in Current Chemistry* 2004, 195–228.

[15] P. Gütlich, *Structure and Bonding* 1981, 83–195.

[16] J.-F. Létard, P. Guionneau, L. Rabardel, J. A. Howard, A. E. Goeta, D. Chasseau, O. Kahn, *Inorganic Chemistry* 1998, 37, 4432–4441.

[17] A. Hauser, *Topics in Current Chemistry* 2004, 49–58.

[18] J. Katriel, R. Pauncz, *Advances in Quantum Chemistry* 1977, 143–185.

[19] S. Matar, P. Guionneau, G. Chastanet, *International Journal of Molecular Sciences* 2015, *16*, 4007–4027.

[20] “Isotope effect,” can be found under https://www.sciencedirect.com/topics/physics-and-astronomy/isotope-effect, 2002 (accessed 18 Sep. 2024).

[21] K. Hosoya, T. Kitazawa, M. Takahashi, M. Takeda, J.-F. Meunier, G. Molnár, A. Bousseksou, *Physical Chemistry Chemical Physics* 2003, *5*, 1682–1688.

[22] P. Gütlich, H. Köppen, H. G. Steinhäuser, *Chemical Physics Letters* 1980, *74*, 475–480.
[23] S. P. Vallone, A. N. Tantillo, A. M. dos Santos, J. J. Molaison, R. Kulmaczewski, A. Chapoy, P. Ahmadi, M. A. Halcrow, K. G. Sandeman, *Advanced Materials* 2019, *31*, 1807334.
[24] S. Rat, M. Mikolasek, J. S. Costá, A. I. Chumakov, W. Nicolazzi, G. Molnár, L. Salmon, A. Bousseksou, *Chemical Physics Letters* 2016, *653*, 131–136.
[25] R. Wordel, F. E. Wagner, *Zeitschrift für Physikalische Chemie* 1989, *164*, 767–772.
[26] A. K. Soper, *Experimental Methods in the Physical Sciences* 2017, 135–211.
[27] Department of Materials Science and Metallurgy - University of Cambridge, can be found under https://www.doitpoms.ac.uk/tlplib/xray-diffraction/peak.php, 2004, (accessed 24. Nov 2024).
[28] G. H. Stout, L. H. Jensen, *X-Ray Structure Determination: A Practical Guide*, Wiley, New York, 1989, 24–25.
[29] D. A. McQuarrie, J. D. Simon, *Physical Chemistry: A Molecular Approach*, University Science Books, Sausalito, 1997, 1181–1203.
[30] G. Rhodes, *Crystallography Made Crystal Clear: A Guide for Users of Macromolecular Models*, 3rd ed., Elsevier, Amsterdam, 2006, 20-30.
[31] T. Brückel, “3. elastic scattering from many-body systems,” can be found under https://www.fz-juelich.de/de/jcns/jcns-2/downloads/brueckel/elastic_scattering_from_many_body_systems_pdf/@@download/file, (accessed 01. Nov. 2024).
[32] “1 principles of X-ray diffraction,” can be found under https://application.wiley-vch.de/books/sample/3527310525_c01.pdf, (accessed 01. Nov, 2024).
[33] L. B. Kong, L. Liu, Z. Yang, S. Li, T. Zhang, C. Wang, *Magnetic, Ferroelectric, and Multiferroic Metal Oxides* 2018, 287–311.
[34] Y. Cao, Z. Huang, Y. Yin, H. Xie, B. Liu, W. Wang, C. Zhu, D. Mandrus, L. Wang, W. Huang, *Materials Today Advances* 2020, *7*, 100080.
[35] S. Mugiraneza, A. M. Hallas, *Communications Physics* 2022, *5*, 95.
[36] Britannica, the Editors of Encyclopaedia, "diamagnetism", https://www.britannica.com/science/diamagnetism, (accessed 01 Nov. 2024) .
[37] Department of Materials Science and Metallurgy - University of Cambridge, can be found under https://www.doitpoms.ac.uk/tlplib/ferromagnetic/types.php, (accessed 01. Nov. 2024).
[38] V. Iacovacci, G. Lucarini, L. Ricotti, A. Menciassi, *Lab-on-a-Chip Fabrication and Application* 2016, 1-56.
[39] R. Nisticò, *Boletín de la Sociedad Española de Cerámica y Vidrio* 2021, *60*, 29–40.
[40] Britannica, the Editors of Encyclopaedia, "Pierre Curie" can be found under https://www.britannica.com/biography/Pierre-Curie, (accessed 01 Nov. 2024).

[41] M. Staruch, *Magnetotransport and Multiferroic Properties of Perovskite Rare-earth Manganites*, PhD Thesis, University of Connecticut, 2013.
[42] A. Chauhan, *Journal of Analytical & Bioanalytical Techniques* 2014, *5*,1-5.
[43] “Crystallographic computing system,” can be found under http://jana.fzu.cz/, 2001 (accessed 14. Oct. 2024).
[44] “Powder diffractometry,” can be found under https://www.stoe.com/powder-diffraction-instruments/, 2024, (accessed 11. Nov. 2024).
[45] “1. components,” can be found under https://www.xhuber.com/en/products/1-components/, (accessed 11. Nov. 2024).
[46] Q. D. Inc., “Physical Property Measurement System (PPMS),” can be found under https://qd-europe.com/at/en/product/physical-property-measurement-system-ppms/,(accessed 18. Sep. 2024).
[47] “Vibrating Sample Magnetometer,” can be found under https://www.dexinmag.com/vibrating_sample_magnetometer, (accessed 19. Sep. 2024)
[48] SWT Physics Department, “Vibrating-sample magnetometer,” can be found under https://en.wikipedia.org/wiki/Vibrating-sample_magnetometer, 2023 (accessed 19. Sep. 2024).
[49] Britannica, The Editors of Encyclopaedia,"Faraday’s law of induction". Encyclopedia Britannica, 26 Oct. 2024, https://www.britannica.com/science/Faradays-law-of-induction. (accessed 20. Sep. 2024).
[50] V. Shukla, *Handbook of Magnetic Hybrid Nanoalloys and their Nanocomposites* 2022, 1–24.
[51] BRUKER OPTIK GmbH, “UNR,” can be found under http://argenta2.chem.unr.edu/downloads/FTIR Tensor Operating Manual.pdf, 2011 (accessed 19. Sep. 2024).
[52] “Mestrenova Manual,” can be found under https://mestrelab.com/wp-content/uploads/2021/09/mnova-2024-05-23-mnova-3.pdf, 2022 (accessed 19. Sep. 2024).
[53] REACH Devices, LLC, “Thin layer chromatography: How to,” can be found under http://www.reachdevices.com/TLC.html, 2010 (accessed 21. Nov. 2024).
[54] S. Kumar, K. Jyotirmayee, M. Sarangi, *International Journal of Pharmaceutical Sciences Review and Research*, 2013, 18(1): 126-132.
[55] S. Aryal, “Thin layer chromatography: Principle, parts, steps, uses,” can be found under https://microbenotes.com/thin-layer-chromatography/, 2023.
[56] J.-F. Létard, P. Guionneau, L. Rabardel, J. A. Howard, A. E. Goeta, D. Chasseau, O. Kahn, *Inorganic Chemistry* 1998, *37*, 4432–4441.
[57] R. M. McCarty, C. Krebs, V. Bandarian, *Biochemistry* 2012, *52*, 188–198.
[58] H. Li, C. Tao, Y. Xie, A. Wang, Y. Chang, H. Yu, S. Yu, Y. Wei, *Green Chemistry* 2021, *23*, 6059–6064.

[59] C. Zhao, Y. Xie, D. Shi, H. Yu, *ChemCatChem* 2023, 15, e202300186.
[60] N. T. Subasi, “Overview of schiff bases,” can be found under https://www.intechopen.com/chapters/84305, 2022 (accessed 29. Nov. 2024).
[61] Z. Hussain, M. Khalaf, H. Adil, D. Zageer, F. Hassan, S. Mohammed, E. Yousif, *Research Journal of Pharmaceutical, Biological and Chemical Sciences*, 2016, *7*, 1008–1025.
[62] G. R. Fulmer, A. J. Miller, N. H. Sherden, H. E. Gottlieb, A. Nudelman, B. M. Stoltz, J. E. Bercaw, K. I. Goldberg, *Organometallics* 2010, *29*, 2176–2179.
[63] T. D. Martins, M. T. Viciosa, M. B. Oliveira, A. Fernandes, J. F. Mano, C. Baleizão, J. P. Farinha, *Progress in Organic Coatings* 2023, *180*, 107552.
[64] J. Zhou, M. Paladino, D. G. Hall, *European Journal of Organic Chemistry* 2022, *41*, e202201050.
[65] “Crystallographic computing system,” can be found under http://jana.fzu.cz/, 2001 (accessed 23. Oct. 2024).
[66] A. Le Bail, H. Duroy, J. L. Fourquet, *Materials Research Bulletin* 1988, *23*, 447–452.
[67] M. Marchivie, P. Guionneau, J.-F. Létard, D. Chasseau, *Acta Crystallographica Section B Structural Science* 2003, *59*, 479–486.
[68] G. A. Bain, J. F. Berry, *Journal of Chemical Education* 2008, *85*, 532.